REPUBLIC OF AZERBAIJAN

On the rights of the manuscript

ABSTRACT

of the dissertation for the degree of Doctor of Science

DESIGN AND PROPERTIES OF THE TOPOLOGICAL INSULATORS AND RELATED MATERIALS BASED ON CHALCOGENIDES AND CHALCOGEN-IODIDES OF SOME HEAVY METALS

Specialty: 3312.01 – Materials Technology

Field of science: Technical

Applicant: **Ziya Sakhavaddin Aliyev**

B a k u – 2021

The work was performed at Azerbaijan State Oil and Industry University, department of "Materials science and processing technologies" and research laboratory "Nanomaterials and nanotechnologies"

Scientific consultant: Prof., corresponding member of ANAS, **Mahammad Baba Babanly**

Official opponents:

Doctor of technical sciences
Faiq Kazım Alaskarov

Doctor of technical sciences, professor
Ali Isa Mammadov

Doctor of technical sciences, professor
Nizami Shayi Ismailov

Doctor of technical sciences, professor
Ibrahim Abulfaz Habibov

Dissertation council ED2.02 of Supreme Attestation Commission under the President of the Republic of Azerbaijan operating at Azerbaijan State Oil and Industry University

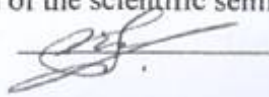Chairman of the Dissertation council: D.Sc., prof., Honored Scientist

Mustafa Baba Babanli

Scientific secretary of the Dissertation council: Ph.D., Assoc. Prof.

Tahir Qaffar Jabbarov

Chairman of the scientific seminar: D.Sc., Assoc. Prof
Qahraman Soyun Hasanov

The defense will be held on 19 __11__ 2021 at 13^{00} at the meeting of the Dissertation council ED2.02 of Supreme Attestation Commission under the President of the Republic of Azerbaijan oper-ating at Azerbaijan State Oil and Industry

Address: AZ 1010, Baku, Azadlig ave. 34.

Dissertation is accessible at the library of Azerbaijan State Oil and Industry

Abstract was sent to the required addresses on "15" october 2021

INTRODUCTION

State-of-the-art and relevance of the topic. The scientific and technological progress in different periods of history has resulted in Industrial Revolutions. The First Industrial Revolution was associated with the emergence of the steam engine, whereas the next two revolutions were associated with the development of automated industry and microelectronics. Today, the world has entered an era of the Fourth Industrial Revolution which is based on high-technologies and artificial intelligence. Each Industrial Revolution brings new requirements for the new materials and technologies realized using those materials. The Fourth Industrial Revolution is an inevitable process mainly due to two reasons: i) a huge amount of information processed on informatics and artificial intelligence, ii) a significant increase in energy consumption, ecological imbalance, and global climate change. Currently, information processing is done in computers based on semiconductor microelectronics. However, their capacity and power are very limited as well as consume quite enough energy. Therefore, the development of novel fast computing systems and low-power electronics is a very hot topic today. On the other side, global climate change requires convert of waste heat to electricity using the convertors like thermoelectrics. The recent progress achieved in physics, chemistry, and materials science opens up new opportunities for the solution of mentioned two global problems.

The most promising material to overcome the former global problem is the *Topological Insulators* (TIs), one of the most important discoveries of the 21st century. With non-trivial surface properties, TIs open up a wide range of opportunities for dissipationless energy transfer and the creation of advanced technologies (spintronics, topotronics, etc.). The existence of plasmonic excitation in the topological surface states (TSS) of TIs, opens up new chances for developing fast, sensitive and portable Terahertz photodetectors.

Regarding the second problem, one of the most promising ways is to create highly efficient semiconductor, photoelectric and thermoelectric materials (TEs) for applications in renewable energy sources. The thermoelectric figure-of-merit (*ZT*) of known materials is not

high enough for a wide range of applications. According to forecasts, the thermoelectric figure-of-merit of TEs should be higher than 2.5 for mass application.

The search for new TIs and TEs as well as the development of scientific and technological foundations for their synthesis are one of the hot topics of materials science and chemistry.

The chaco(halo)genides of Ge and As subgroup elements are of great importance as advanced materials. Homologous series of $n(A^{IV}B^{VI}) \cdot n(A^V_2B^{VI}_3)$ compounds formed in $A^{IV}B^{VI}$-$A^V_2B^{VI}_3$ (A^{IV}=Ge, Sn, Pb; A^V=Sb, Bi; B^{VI}-Te) systems are narrow-gap semiconductors and are of special importance both as TEs and TIs. Doping of Rare Earth Elements (REE) into their crystal structure, the thermal conductivity decreases depending on the mass and ionic radii of the REE atoms, consequently the ZT coefficient increases.

The creation of magnetic analogous of $n(A^{IV}B^{VI}) \cdot n(A^V_2B^{VI}_3)$ homologous phases attracts huge interest in last years for spintronics, topotronics, and spin caloritronics. Until 2019, magnetic topological insulators (MTIs) have only been realized using doping of trivial TIs with $3d$ transition metals (TM); however, due to the inhomogeneous distribution of the magnetic elements, the T_c and other parameters were not high enough in all these cases. An intrinsic magnetic topological insulator - a stoichiometric well ordered magnetic compound - could be an ideal solution to these problems. In 2019, the first and only intrinsic 3D antiferromagnetic TI (AFMTI) - $MnBi_2Te_4$ was synthesized, solving the inhomogeneity problem. As the first-ever observed AFMTI, this compound opens wide opportunities for the experimental exploration of quantum anomalous Hall effect, axion electrodynamics, Majorana hinge modes, and other exotic phenomena. As an *axion insulator,* it is expected to use in the detection of *axions* – the theoretical particles that made dark matter. The ferromagnetic septuple blocks of this compound make also it an ideal platform to design topological nontrivial heterostructures.

$A^VB^{VI}Hal$ (Hal=Cl, Br,I; B^{VI}-S,Se,Te) type chalcohalogenid phases are semiconductors having photovoltaic, ferroelectric, piezoelectric, and thermoelectric properties. Another exotic physical effect observed in these compounds is a giant 3D Rashba spin-splitting of sur-

face states. The unusual toroidal 3D Fermi surface caused by Rashba type spin-splitting of BiTeI may open a pathway for the realization of exotic physical systems for topotronics and spintronics.

One of the important stages in the design of multi-component inorganic materials is the study of the phase equilibria in the relevant systems. The phase diagram is a geometric expression of the thermodynamic equilibrium state of the system and allows to directly determine the formation of new (non)stoichiometric phases, their primary crystallization and homogeneity fields, phase transformations, etc. The totality of these data underlies the development of methods for the synthesis and growth of single crystals.

The literature survey shows that the phase diagram of some TM-A^V-Te, REE-A^V-Te, REE-A^{IV}-A^V-Te, and A^V-B^{VI}-Hal have not been studied or studied along only some sections, or although studied for the entire composition range, the reported data are quite contradictory. Therefore, to confirm those data and to search new phases the (re)investigation of their phase diagrams is always important.

Despite the Mn-Bi-Te system attracts a lot of interest in the last few years, its phase diagram has not been studied yet. Taking into account that the $MnBi_2Te_4$ compound found in this system along the $MnTe$-Bi_2Te_3 quasi-binary section and is analogous to well-known $A^{IV}A^V_2Te_4$-type compounds, the formation of the $A^{IV}A^V_4Te_7$ and $A^{IV}A^V_6Te_{10}$-type compounds are expected. Thus, the investigation of the $MnTe$-Bi_2Te_3 phase diagram is of particular interest.

Due to mentioned chalcogenide materials will be used in many technological devices operated in the real environment, the experimental study of their surface chemical reactivity toward air and water is very crucial. Determination of some mechanical properties plays also a crucial role in their potential application in flexible electronics and nanoelectromechanical (NEMS) devices.

The aim of the work. The main aim of this work is the search, design, characterization and creation of synthesis and crystal growth fundamentals of new multifunctional chalco(halo)genide materials with trivial and magnetic topological insulating, Rashba spin-splitting, photovoltaic-ferroelectric, and thermoelectric properties. To achieve this aim the following tasks were set and resolved:

5

– An investigation of the phase diagrams of the ternary YbTe-Sb$_2$Te$_3$(Bi$_2$Te$_3$)-Te, Sb-S(Se)-I, Bi-S(Se)-I, Mn-Bi-Te and quaternary YbTe-Sb$_2$Te$_3$-Bi$_2$Te$_3$, YbTe-SnTe-Sb$_2$Te$_3$(Bi$_2$Te$_3$), Bi$_2$Se$_3$-Bi$_2$Te$_3$-BiI$_3$, 3PbSe-Bi$_2$Te$_3$↔3PbTe-Bi$_2$Se$_3$ systems;

– Fundamentals of the synthesis technologies of newly designed stoichiometric and nonstoichiometric solid solution phases based on plotted phase diagrams;

– Elaboration and identification of new phases and, X-ray study of their structural features;

– Study of the surface chemical reactivity of single crystals some TIs phases toward oxygen, water, and carbon monoxide at room and high temperatures;

– Determination of some mechanical properties of single-crystalline TIs to determine their potential applications in flexible electronics and NEMS devices;

– Study of the electronic band and surface properties of the elaborated TIs phases in the framework of international collaboration;

Research methods. The experimental analyses were done using DTA, XRD, SEM-EDS, Raman spectroscopy, X-ray photoemission spectroscopy (XPS), Nanoindentation measurements as well as ARPES and SARPES techniques. DTA measurements were done on NETZSCH 404 F1 Pegasus DSC equipment, XRD data were collected in a Bruker D2 Phaser and D8 ADVANCE diffractometers. SEM-EDS analyses were carried out using a TESCAN VEGA3 SBH Scanning Electron Microscope equipped with ThermoScientific Ultra-Dry Compact EDS detector and FEI QuantaTM 250 SEM equipped with Oxford Instruments detector.

Raman characterizations of the Mn-Bi-Te compounds were done using Nanofinder 30 3D confocal microspectrometer. The surface chemical reactivity of TIs single crystals was investigated by XPS using synchrotron radiation. Nanoindentation tests of the Bi$_2$Te$_3$ were performed with an Anton Paar Nano Indenter equipped with Berkovich tip. The surface and band electronic properties of the TIs single crystals were studied within the international collaboration.

Scientific novelty. In the dissertation work, the new phases based

on mentioned-above systems having trivial and magnetic topological surface states, Rashba-type spin-splitting, photovoltaic-ferroelectric and thermoelectric properties have been elaborated and characterized and, novel results regarding the scientific and technological fundamentals for their synthesis and single crystal growth obtained:

– The phase diagrams of isopleth and isothermal sections as well as liquidus surface projection of the mentioned systems were plotted. The primary crystallization and homogeneity fields, the type and coordinates of the in- and monovariant equilibria were identified. The crystal lattice parameters of all the newly synthesized phases were calculated from XRD data.

– The existence of the ternary $YbSb_2Te_4$, $YbSb_4Te_7$, $YbBi_2Te_4$, $YbBi_4Te_7$, and $YbSnTe_2$ compounds reported earlier in the Yb-based systems were not confirmed, whereas the continuous or wide solid-solubility fields based on starting compounds were revealed.

– The new Te↔Se anion-substituted solid-solution series was revealed in the BiSeI-BiTeI section of the quasi-ternary Bi_2Se_3-Bi_2Te_3-BiI_3 and in reciprocal $3PbSe$-Bi_2Te_3↔$3PbTe$-Bi_2Se_3 system. In addition, new $MnBi_4Te_7$ and $MnBi_6Te_{10}$ compounds belong to $(MnTe) \cdot n(Bi_2Te_3)$ homologous series were synthesized in the Mn-Bi-Te system along the $MnTe$-Bi_2Te_3 quasi-binary section, their crystal structures and Raman characteristics were done.

– The synthesis and single crystal growth methods of newly revealed materials were prepared using the plotted phase diagrams of the respective three- and four-component systems. Some earlier known phase diagrams of some systems host functional phases including TIs were reinvestigated using new approaches and then single crystals of those materials were grown using obtained data.

Electronic band and surface features of the stoichiometric $PbBi_4Te_7$, $SnBi_2Te_4$, $SnBi_4Te_7$, $GeBi_2Te_4$ etc. compounds from $n(A^{IV}Te) \cdot m(Bi_2Te_3)$ homologous series as well as $PbBi_2Te_2Se_2$, $PbBi_2Te_{1.4}Se_{2.6}$, $PbBi_4Te_4Se_3$ and $PbBi_4Te_6Se$ phases form $PbBi_2Te_{4-x}Se_x$ and $PbBi_4Te_{7-x}Se_x$ solid-solutions were studied in the framework of international collaboration.

– The novel manganese bismuth tellurides are found to be the

first intrinsic antiferromagnetic topological insulators. The antiferromagnetic→ferromagnetic transition was found to occur in the MnBi$_6$Te$_{10}$ compound.

– The surface chemical reactivity and topological robustness of the Bi$_2$Se$_3$, Bi$_2$Te$_3$, GeBi$_2$Te$_4$, SnBi$_4$Te$_7$, and PbBi$_6$Te$_{10}$ single crystals toward O$_2$, H$_2$O, and CO were studied by XPS.

– The Young's modulus, fracture toughness and hardness of the single-crystalline Bi$_2$Te$_3$ were determined to establish its possible application in flexible electronics and NEMS devices.

The main theses are presented for defense.

– The phase diagrams of the ternary YbTe-Sb$_2$Te$_3$(Bi$_2$Te$_3$)-Te, Sb-S(Se)-I, Bi-S(Se)-I, Mn-Bi-Te and quaternary YbTe-Sb$_2$Te$_3$-Bi$_2$Te$_3$, YbTe-SnTe-Sb$_2$Te$_3$(Bi$_2$Te$_3$), Bi$_2$Se$_3$-Bi$_2$Te$_3$-BiI$_3$ and 3PbSe-Bi$_2$Te$_3$↔3PbTe-Bi$_2$Se$_3$ systems;

– Synthesis and growth of bulk single crystals of the new phases based on phase diagrams;

– Crystal structure features of the obtained new compounds and solid solutions phases;

– Topological insulator properties of the n(A^{IV}Te)·m(Bi$_2$Te$_3$) homologous series compounds and phases of the 3PbSe-Bi$_2$Te$_3$↔3PbTe-Bi$_2$Se$_3$ reciprocal system with variable compositions;

– Raman characteristics and antiferromagnetic topological insulator properties of new manganese bismuth tellurides;

– The surface chemical reactivity and topological robustness of the Bi$_2$Se$_3$, Bi$_2$Te$_3$, GeBi$_2$Te$_4$, SnBi$_4$Te$_7$, and PbBi$_6$Te$_{10}$ single crystals;

– Some mechanical properties of the single-crystalline 3D TI Bi$_2$Te$_3$;

Theoretical and practical significance. The fundamental results related to the theoretical and technological foundations for the elaboration of new multifunctional chalcogenide and chalcoidide phases are a significant contribution to the modern material science of advanced materials such as TIs, TEs, and similar materials.

Plotted phase diagrams, crystallographic parameters of new phases, and other studied electronic and surface properties are fundamental physical parameters and can be included in the relevant databases

and handbooks. The set of studied properties of each material is very important to determine its possible application field and condition.

The phase diagrams of the studied systems are essential when focusing on the chemistry, i.e., synthesis and crystal growth of functional materials. Knowledge on phase equilibria is also crucial to understand the *composition-microstructure-properties* relationship.

Numerous single-crystalline chalcogenide materials were obtained in this work and studied as 3D TIs. They have been confirmed as the most promising materials for the realization of spintronic and low-power electronic devices, quantum computers as well as new terahertz detectors in near future.

As the first AFMTI, $MnBi_2Te_4$ and $MnBi_2Te_4 \cdot nBi_2Te_3$ phases are expected to be implemented soon for the realization of many exotic phenomena such as quantum anomalous Hall and other magnetoelectric effects, axion electrodynamics, etc.

The novel phases found in the $YbTe$-$Sb_2Te_3(Bi_2Te_3)$-Te, $YbTe$-Sb_2Te_3-Bi_2Te_3, and $YbTe$-$SnTe$-$Sb_2Te_3(Bi_2Te_3)$ systems can be used as TEs with low-thermal conductivity. In addition, the spinodal phase transformation revealed in the $YbTe$-$SnTe$ system can be used to obtain nanostructured $Yb_{1-x}Sn_xTe$ solid-solution materials.

The γ_1 phase revealed in the $BiSeI$-$BiTeI$ system can be used in multifunctional devices as an optimized photo- and ferroelectric material while the γ_2 phase can be implemented as a Rashba semiconductor with optimized properties.

Approbation. The main results of the dissertation were presented and disseminated in the following international conferences: Int. conf. HighMatTech-2009, Kyiv-2009; IX int. Kurnakov conf. on physico-chemical analysis. Perm-2010; VIII Int. conf. on the electronic process in organic and inorganic materials, Ivano-Frankovsk-2010; XVIII Ukr. conf. on inorganic chemistry, Kharkiv-2011; II int. sci.-tech. conf. "functional and construction materials, Donetsk-2011; All-Russ. conf. "solid-state chemistry and functional materials", Ekaterinburg-2012; XIV int. sci.-tech. conf. "high-tech chemical technologies-2012", Tula-Yasnaya Polyana-Kulikovo Pole-2012; VI All-Russ. conf. "Physicochemical processes in condensed matters and interphases", Voronezh-2012; X int. Kurnakov meeting on physical

and chemical analysis, Samara-2013; XII int. conf. on crystal chemistry of intermetallic compounds, Lviv-2013; II int. Turkic world conference on chemical sciences and technologies, Skopje-2016; XV int. conf. on physics and technology of thin films and nanosystems, Ivano-Frankivsk-2015; XV All-Russ. conf. "high-purity substances and materials. Obtaining, analysis, application", Nizhny Novgorod-2015; VII All-Russ. conf. "Physicochemical processes in condensed matters and interphases - FAGRAN-2015", Voronezh-2015; Int. conf. "multifunctional chemical materials and technologies", Tomsk-2015; All-Russ. sci. conf. "II Baikal Materials Science Forum", Ulan-Ude-2015; XIII int. conf. on theory and application of fuzzy systems and soft computing, Warsaw-2018; I int. conf. on actual problems of chemical engineering - APCE-2020, Baku-2020.

Publications. 75 research articles on the topic of the dissertation, including 57 articles in peer-reviewed scientific journals (44 of them in Science Citation Index/Expanded (SCI/SCIE) journals), and 18 abstracts of reports in the conference proceedings were published. According to the "Google Scholar" bibliographic database, these published papers were cited by more than 2000.

Organization and research projects where the work was performed. This work was performed at ASOIU. The research works are given in IV, VI and VIII chapters were partially supported by the Science Development Foundation under the President of the Republic of Azerbaijan, grant № EIF-2011-1(3)-82/69/4-M-50; grant № EIF/MQM/Elm-Tehsil-1-2016-1(26)-71/01/4-M-33 and grant № EİF-BGM-4-RFTF-1/2017-21/04/1).

Volume and structure. The dissertation is 315 pages and contains Introduction, 10 chapters (Chapter I-18 p., II-23 p., III-25 p., IV-45 p., V-33 p., VI-22 p., VII-17 p., VIII. -16 p., IX-19 p., X-23 p.), Results, 450 References. 180 pages from the total volume of the dissertation are main text, while the other parts – are figures (130 figures), tables (20 tables), and appendices (11 pages).

Author contribution. The author was responsible for the conceptualization of the dissertation topic, the implementation of the experimental works, an analysis of the results, the writing of research papers, and the preparation of the dissertation.

MAIN CONTENT OF THE WORK

The **Introduction** shows the state-of-the-art and relevance of the dissertation topic, the aim and scientific novelty of the results obtained, the theoretical and practical significance, approbation, and the structure of the dissertation.

Chapter I describes the literature review on trivial and magnetic TIs, TEs, Rashba semiconductors and photovoltaic-ferroelectric materials. Herein, the scientific foundations of the topological state of matter, thermoelectric conversion, Rashba spin-splitting effect, and photovoltaic-ferroelectric phenomena are explained. In addition, it was shown that complex chalcogenide and chalcohalide phases which exhibit these properties are perspective advanced functional materials and have potential application fields.

Chapter II provides a comparative analysis of the available up to date literature data on phase equilibria, crystal structure and electronic properties of intermediate phases in the A^V-Te, A^{IV}-A^V-Te, and A^V-B^{VI}-I systems to properly organize and realize experimental researches. This chapter describes the formation and layered crystal structure features of binary $A^V_2Te_3$ and $n(A^V_2){\cdot}m(A^V_2Te_3)$, as well as ternary $n(A^{IV}Te){\cdot}m(A^V_2Te_3)$ homologous series of compounds formed in the A^V-Te and A^{IV}-A^V-Te systems, respectively. Here, the formation of each building block of crystal structure, their stacking sequence, and possible use in new designs are explained. A literature review on the transport and other electronic properties of these binary and ternary phases both pristine and doped form as well as the structure↔properties correlation is explained, consequently, these materials are shown to be tunable by chemical design. This chapter also describes the phase equilibria in the ternary A^V-B^{VI}-I systems and the physical properties of their ternary chalcoidide phases.

At the end of the chapter, the design of new functional phases, synthesis of the stoichiometric and solid solution phases, selection, and study of appropriate ternary and quaternary systems for the development of synthesis and crystal growth technologies are justified.

Chapter III provides a brief review on the general principles of the synthesis of stoichiometric compounds and alloys in condensed systems, their classification, and some features of the complex physi-

cochemical analysis of the corresponding element systems. Herein, the classification of synthesis methods for chalcogenide and chalcohalogenide phases is given and the choice of synthesis methods for the studied system is shown. Synthesis of the binary and more complex telluride phases were done in the evacuated (~10^{-3} Pa) silica or niobium (for Yb alloys) containers by co-melting of elements with high purity. The synthesis of chalcoidides was carried out in two-zone furnaces by the co-melting of elemental components, i.e., the corresponding metal, solid-state iodine, or the corresponding iodide and chalcogenide phase. The synthesis and annealing regimes of all telluride and chalcoiodide phases are given in the relevant chapters of the dissertation.

This chapter provides a classification of the major synthesis methods for single-crystalline materials, their working principles and justification of the method selection for growing single crystals of different multi-component chalcogenide and chalcohalogenide phases.

Chapter IV describes the new obtained results regarding the phase diagrams and phase formation features in the quasi-ternary systems YbTe-Sb$_2$Te$_3$-Te, YbTe-Bi$_2$Te$_3$-Te, YbTe-Sb$_2$Te$_3$-Bi$_2$Te$_3$ and YbTe-A$^V_2$Te$_3$-SnTe. The literature review shows that the phase equilibria in Yb-A^V-Te systems have been studied by only one group of authors and they showed the existence of several ternary compounds. However, among them, there is no system that the phase diagram is reliable enough, and the reported data are often contradictory. Due to YbTe-A$^V_2$Te$_3$ isopleth sections are boundary one for the quasi-ternary YbTe-A$^V_2$Te$_3$-SnTe and YbTe-Sb$_2$Te$_3$-Bi$_2$Te$_3$ systems, their throughput investigations are crucial. Therefore, the phase equilibria in the ternary Yb-A^V-Te systems were studied experimentally along the YbTe-Sb$_2$Te$_3$-Te and YbTe-Bi$_2$Te$_3$-Te quasi-ternary planes.

Quasi-ternary system YbTe-Sb$_2$Te$_3$-Te. The phase diagram of the YbTe-Sb$_2$Te$_3$ isopleth (Fig.1a) of this quasi-ternary system belongs to eutectic type (type V within the Roseboom's classification) with the invariant points lying at 78 mol% Sb$_2$Te$_3$ and 860 K. At the eutectic temperature the solubility limit of YbTe in Sb$_2$Te$_3$ (β-phase) is achieved at 18 mol%, while the observed solubility limit of Sb$_2$Te$_3$ in YbTe (α-phase) is extremely small (no more than ~1 mol%).
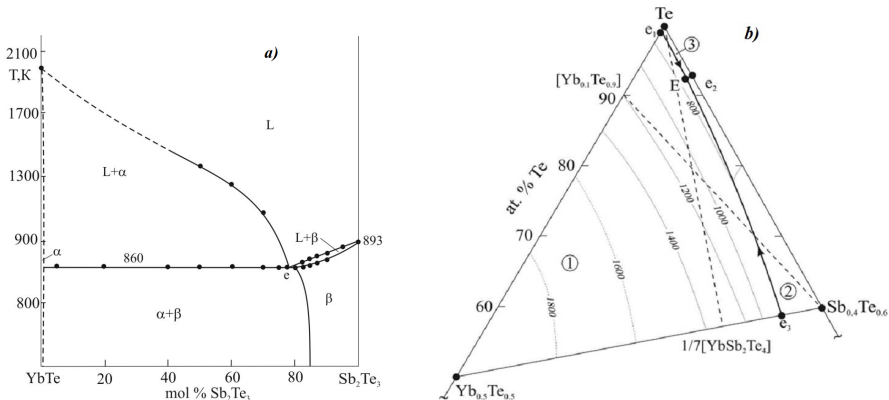
Figure 1. (*a*), the phase diagram of the YbTe-Sb₂Te₃ system and (*b*), liquidus surface projection of the YbTe-Sb₂Te₃-Te system (primary crystallization fields: 1, α (YbTe); 2, β (Sb₂Te₃); 3, Te)

the system, the existence of the ternary compounds YbSb₂Te₄ and YbSb₄Te₇ reported earlier was not confirmed. The phase compositions of the alloys having 50 and 33.3 mol% YbTe are found to be biphasic made of α+β heterogeneous mixture.
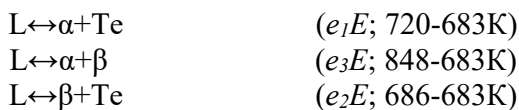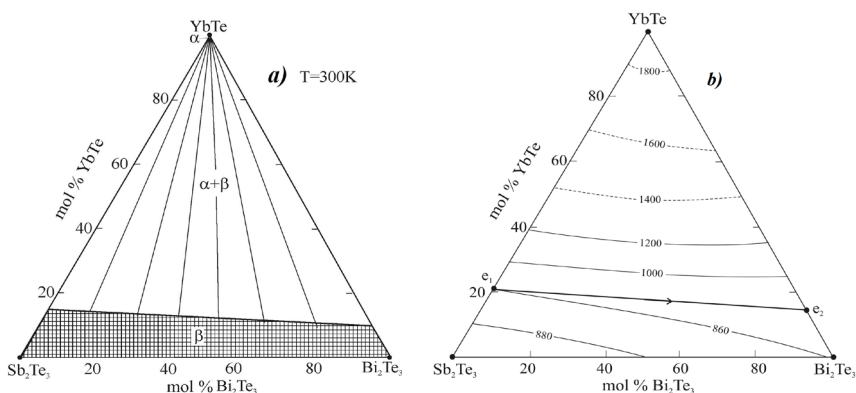
The liquidus surface projection of the system (Fig. 1*b*) was constructed from experimental results up to 1400 K and then by extrapolation up to 1800 K. As can be seen, it relates to the invariant eutectic type and consists of the fields of the primary crystallization of elemental tellurium, α- and β-phases. The primary crystallization fields are bordered by the following monovariant eutectic reactions:

$$L \leftrightarrow \alpha + Te \qquad (e_1E; \ 720\text{-}690 \text{ K})$$
$$L \leftrightarrow \alpha + \beta \qquad (e_3E; \ 860\text{-}690 \text{ K})$$
$$L \leftrightarrow \beta + Te \qquad (e_2E; \ 695\text{-}690 \text{ K})$$
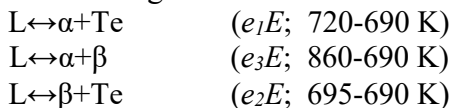
It should be noted that no other invariant equilibria, including those reported in the literature were detected during the present investigation. Two isopleth sections, [Yb₀.₁Te₀.₉]-Sb₀.₄Te₀.₆ and [YbSb₂Te₄]-Te were studied to determine the crystallization sequence and the exact position of the monovariant lines in this system and to plot the liquidus surface projection.

Quasi-ternary system YbTe-Bi₂Te₃-Te. The phase diagram of this system (Fig. 2*a*) also belongs to type V within Roseboom's classification. Eutectic point found to lie at 85 mol% Bi₂Te₃ and 848 K.

13

At eutectic equilibrium temperature the solubility limit of YbTe in Bi_2Te_3 (β-phase) is achieved at 13 mol%, whereas the solubility limit of Bi_2Te_3 in YbTe (α-phase) is found to be less than ~1 mol%. The plotted phase diagram exhibit a completely different phase equilibria scheme from that reported earlier. Intermediate alloys having 50 and 33.3 mol% YbTe those according to the stoichiometric composition of $YbBi_2Te_4$ and $YbBi_4Te_7$ are found to have biphasic content made of α- and β-phases. In addition, a comparative analysis of all the XRD patterns for intermediate alloys shows that no any alloy within this system crystallizes Th_3P_4-type cubic or tetradymite type 21-layered structure as already reported by other authors. One can be seen from the liquidus surface projection of the quasi-ternary system (Fig. 2a), it has an invariant eutectic type diagram and featured by three primary crystallization fields (Te, α- and β-phases) bordered by the following monovariant reactions:

$$L \leftrightarrow \alpha + Te \qquad (e_1E; \; 720\text{-}683K)$$
$$L \leftrightarrow \alpha + \beta \qquad (e_3E; \; 848\text{-}683K)$$
$$L \leftrightarrow \beta + Te \qquad (e_2E; \; 686\text{-}683K)$$

Two isopleth sections studied within the system - ($[Yb_{0.1}Te_{0.9}]$-$Bi_{0.4}Te_{0.6}$ and $[YbBi_2Te_4]$-Te) confirm clearly the revealed phase formation scheme, crystallization fields, and all the equilibrium reactions within the quasi-ternary system.
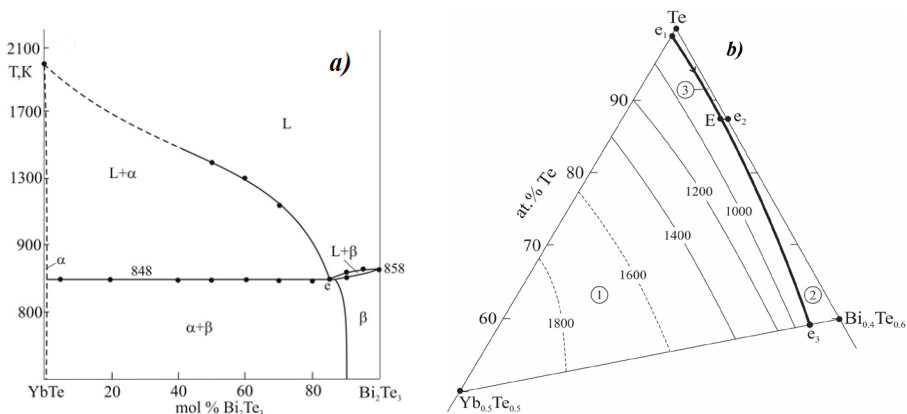
Figure 2. (a), the phase diagram of the $YbTe$-Bi_2Te_3 system and (b), liquidus surface projection of the $YbTe$-Bi_2Te_3-Te system (primary crystallization fields: 1, α; 2, β; 3, Te)

Quasi-ternary system YbTe-Sb₂Te₃-Bi₂Te₃. The phase equilibria in the quaternary Yb-Sb-Bi-Te system were studied along with the YbTe-Sb₂Te₃-Bi₂Te₃ sub-system. The phase diagram of two isothermal sections at 300 and 850 K, the projection of the liquidus surface as well as three isopleth sections were plotted from experimental data. As can be seen from 300 K isothermal (Fig. 3*a*), no any intermediate quaternary compound is detected in this system. The observed homogeneity field of β-phase is ranging from 10 to ~5 mol% YbTe at room temperature along the Sb₂Te₃-Bi₂Te₃ system. With increasing temperature from 300 K up to 850 K this field slightly extending and ranges from 13 to 18 mol% YbTe.

The phase diagram of the YbTe-Sb₂Te₃-Bi₂Te₃ system (Fig. 3*b*) belongs to monovariant eutectic type because of one of the boundary binary systems involved in this quasi-ternary system is a "cigar" type isomorphous, whereas the other two are of the simple eutectic type. As can be seen, the liquidus surface (Fig. 3*b*) consists of two fields corresponding to the primary crystallization of the β and α-phase. The only monovariant eutectic equilibrium L↔YbTe+β vary in a narrow temperature range from 848 to 860 K. Within the system, isopleth sections YbTe-SbBiTe₃, Sb₂Te₃-[YbBi₂Te₄] and Bi₂Te₃-[YbSb₂Te₄] were studied in order to determine the exact position of the monovariant line, the boundaries of the primary crystallization fields and the homogeneity fields of α- and β-phases.

Figure 3. (*a*), an isothermal section of the YbTe-Sb₂Te₃-Bi₂Te₃ system at 300 K and (*b*), liquidus surface projection

Quasi-ternary system YbTe-Sb₂Te₃-SnTe. The phase equilibria in the quaternary Yb-Sn-Sb-Te system were studied with the YbTe-SnTe-Sb₂Te₃ sub-system. The phase diagram of binary system SnTe-YbTe was reported earlier and YbSnTe₂ compound was found in this system which melts at 1335 K. We have attempted to synthesize this compound, i) by melting stoichiometric amounts of the elementary components; ii) from pre-synthesized binary YbTe and SnTe. But, in both cases, the biphasic equilibrium of the two cubic phases was identified even after annealed for about 1500 h at 800 K. Due to the disagreement between literature data and results combined from our preliminary experiments, reinvestigation of this system was also carried out. Apparently, it is a quasi-binary one (Fig. 4*a*) and belongs to type I within Roseboom's classification above 1000 K. The phase diagram of this system is completely different from those reported one. Due to both YbTe and SnTe have very close lattice parameters and the same space group, they are completely miscible in the solid-state and form continuous solid solutions (α-phase) below solidus. According to XRD and SEM-EDS data of intermediate alloys, it was found that a spinodal-type phase decomposition of this solid solution occurs below ~950 K in the compositional range of 3-65 mol% SnTe. Subsequently, new α₁- and α₂-solid solutions fields appear from room temperature up to ~950 K. Thus, the existence of the ternary
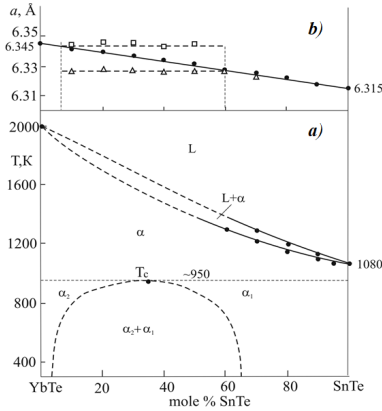
Figure 4. (*a*) YbTe-SnTe phase diagram and (*b*) unit cell parameters for the α- (●), α₁- (Δ) and α₂-phase (□) in the samples annealed at 1000 and 700 K, respectively.

YbSnTe$_2$ compound was not confirmed. The isothermal sections of the system YbTe-Sb$_2$Te$_3$-SnTe at 300 (Fig. 5a) and 700 K were constructed. Four different solid solution fields (α_1-, α_2-, β- and γ-phases) were found at 300 and 700 K. The interaction of these phases leads to the formation of various bi- and triphasic regions where the α_2-phase plays a decisive role. The liquidus surface projection (Fig. 5b) consists of four fields corresponding to the primary crystallization of the α_1 (below ~950 K, $\alpha(\alpha_2)$, γ and β-phases. These fields are bordered by monotectic lines and invariant points. The mutual solubility of α_1- and α_2-phases increases with increasing temperature and above ~950 K they are completely dissolved in each other. Subsequently, the border between crystallization fields of α_1- and α_2-phases is completely disappeared and transform into the primary crystallization field of α-phase (point K). 900 and 1000 K isothermals of the system show that different solid-phase areas (i.e. β, γ-, $\beta+\gamma$, $\alpha_2+\beta$, $\alpha_2+\gamma$ and $\alpha_2+\beta+\gamma$) exist at 300 and 700 K completely disappeared with increasing temperature and liquid or solid-liquid coexistence phase areas appears instead of them at 900 K. Ultimately, new seven different phase regions were observed at 900 K. With the increasing temperature up to 1000 K, the liquid phase continuous shrinks towards the SnTe. Subsequently, one solid phase (α), one liquid (L) and one solid-liquid coexistence ($\alpha+L$) regions exist at this temperature.
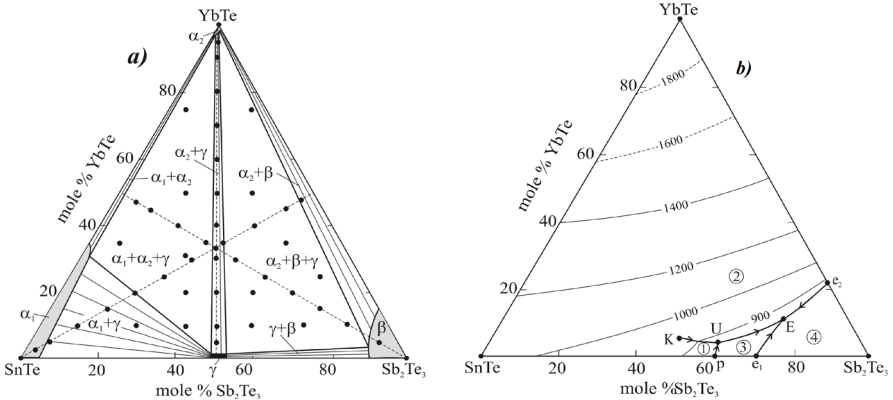
Figure 5. (a), 300 K isothermal of the YbTe-SnTe-Sb$_2$Te$_3$ system and (b), liquidus surface projection (primary crystallization fields: 1, α_1; 2, α (α_2); 3, γ; 4, β)

Isopleth sections, YbTe-SnSb$_2$Te$_4$, SnTe-[YbSb$_2$Te$_4$] and Sb$_2$Te$_3$-[YbSnTe$_2$] were studied to determine the crystallization sequence and the exact position of the monovariant equilibria as well as boundaries of the primary crystallization fields and homogeneity fields.

Quasi-ternary system YbTe-Bi$_2$Te$_3$-SnTe. The phase relationship in the quaternary Yb-Sn-Bi-Te system was investigated along the YbTe-SnTe-Bi$_2$Te$_3$ sub-system. Three different solid solubility fields (α_1-, α_2- and β-) based on SnTe, YbTe and Bi2Te3, respectively, were observed at 300 (Fig. 6*a*) and 800 K. No new quaternary compound was detected in the system. Ultimately, three three-phase and four two-phase equilibrium regions were found in this system at 300 K. The homogeneity fields of α_1-phase along the YbTe-SnTe system is 35 mol% at 300 K and it penetrates into the composition triangle up to ~5 mol%. The homogeneity fields of β-phase from the same side are found to be ~10 mol%, whereas is ~25 mol%from the SnTe-Bi$_2$Te$_3$ side. Solid solubility based on YbTe (α_2-phase) does not exceed ~2-3 mol%. Upon increasing temperature from 300 to 800 K, the homogeneity fields of α_1- and α_2-phases are extended toward each other, consequently, the biphasic $\alpha_1+\alpha_2$ field is narrowed, moreover, the biphasic α_2+SnBi$_2$Te$_4$ appears.

The liquidus surface projection of the system (Fig. 6*b*) consists of five fields corresponding to the primary crystallization of the $\alpha(\alpha_2)$ ($\leq$~950 K), α_1, SnBi$_2$Te$_4$, SnBi$_4$Te$_7$ and β -phases. As can be seen, the primary crystallization areas of the $\alpha(\alpha_2)$ phases are very wide, which makes it possible to obtain bulk single crystals of these phases with different stoichiometries by directed crystallization. The types and coordinates of invariant equilibria, including liquid compositions, and the types and temperature intervals for the monovariant equilibria were determined. The isothermal sections at 900 and 1000 K of the phase diagram show that the phase areas exist at 300 and 800 K completely disappear with increasing temperature up to 900 K and instead of them, new three monophasic (α_1, α_2 and L), three biphasic (α_1+L, α_2+L and $\alpha_1+\alpha_2$) and one triphasic ($\alpha_1+\alpha_2+$L) equilibrium areas appear. Upon increasing temperature up to 1000 K, the liquid phase continuously shrinks towards SnTe and therefore, several phase areas that exist at 900 K completely disappear at 1000 K.
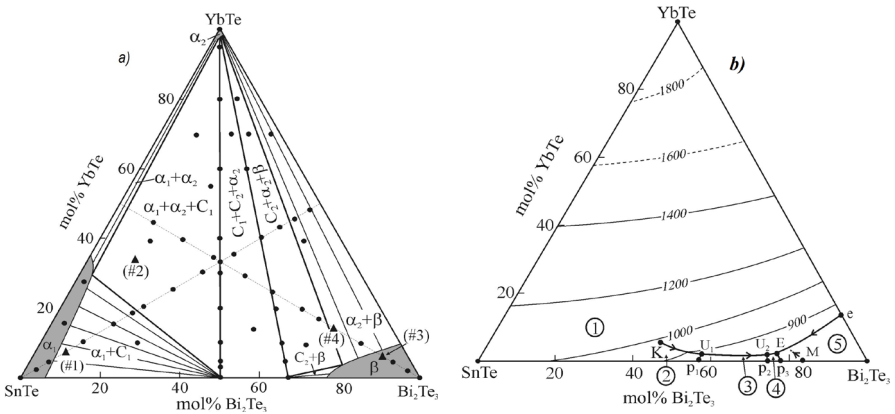
Figure 6. (*a*), 300 K isothermal of the YbTe-SnTe-Bi$_2$Te$_3$ system and (*b*), liquidus surface projection (primary crystallization fields: 1, α(α$_2$); 2, α$_1$; 3, SnBi$_2$Te$_4$; 4, SnBi$_4$Te$_7$; 5, β)

Consequently, only one solid phase (a), one liquid phase (L) and one solid-liquid phases coexistence (aþL) regions exist at this temperature. The isopleth sections YbTe-SnBi$_2$Te$_4$, SnTe-[YbBi$_2$Te$_4$] and Bi$_2$Te$_3$-[YbSnTe$_2$] were also studied.

Chapter V discusses the new results regarding the phase equilibria and phase formation features in the ternary A^V-B^{VI}-I systems.

The ternary system Sb-S-I. Two quasi-binary, three isopleth sections, 300 K isothermal section, and liquidus surface projection of this system were experimentally revised. The quasi-binary Sb$_2$S$_3$-SbI$_3$ section plotted in our work agrees well with that reported earlier. The existence of the SbSI compound and eutectic equilibria made by this compound was confirmed. The phase diagram of the quasi-binary SbI$_3$-S section was plotted. It was found to be a simple eutectic type. The eutectic point lies at ~97 at.% S and 287 K. Five three-phase equilibrium areas were found in the Sb-S-I system at 300 K. All phases of the system are revealed to be in equilibrium with SbSI indicates that it plays a key role in the distribution of the phase areas in the subsolidus area. No solid solution fields as well as no other ternary compound trace were detected during the present investigation.

The liquidus surface (Fig. 7) consists of six primary crystallization fields corresponding to two binary and one ternary compound and three elemental components. The primary crystallization field of the

SbSI is quite large and occupies a considerable part of the total area of the composition triangle, which provides a variety of compositions of the melts for growing single crystals of the SbSI compound. The largest primary crystallization field belongs to elemental antimony. Except for the elemental sulfur, the primary crystallization fields of the Sb_2S_3, SbI_3 binary compounds and elemental iodine also take place in the large area. Two wide immiscibility fields were detected in this system. Among them, the first one (L_1+L_2) starts from the Sb-I system (m_3m_3') and joins to the immiscibility field of the Sb-Sb_2S_3 subsystem (m_1m_1') over the Sb-SbSI section (m_4m_4'). It almost covers the primary crystallization field of antimony in the Sb-SbI_3-Sb_2S_3 subsystem. Within this composition range, the primary crystallization of antimony takes place by invariant $L_1 \leftrightarrow L_2+Sb$ monotectic reaction. The second immiscibility field (L_2+L_3) starts from the Sb_2S_3-S subsystem (m_2m_2') and spreads into the Sb_2S_3-SbSI-S subsystem. The monovariant eutectic (e_5E_3) curve passes through this field and splits into two e_5M and $M'E_3$ curves, subsequently, appears as a horizontal line (MM') at 630 K that reflects the quadriphase monotectic equilibria M. The primary crystallization field of elemental sulfur and some
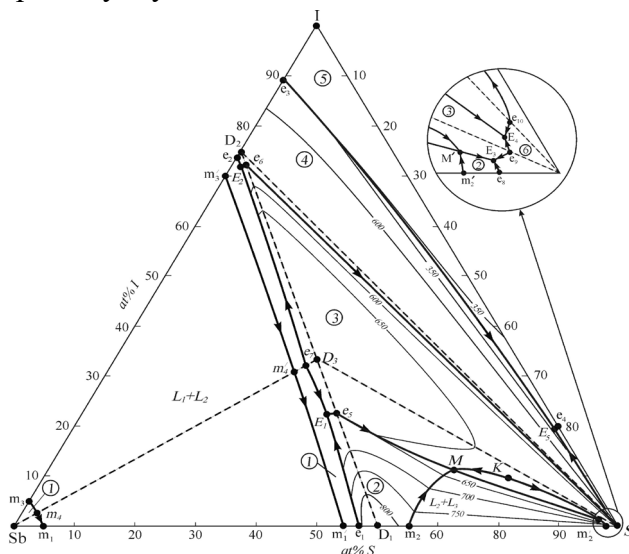

Figure 7. The liquidus surface projection of the Sb-S-I system (primary crystallization fields: 1, Sb; 2, Sb_2S_3; 3, SbSI; 4, SbI_3; 5, I_2; 6, S)

20

Table 1.

Invariant equilibria in the Sb-S-I system

№	Point in Fig. 7	Equilibrium	composition, mol%			T,K
			Sb	S	I	
1	D_1	L↔Sb$_2$S$_3$	40	60	-	830
2	D_2	L↔SbI$_3$	25	-	75	443
3	D_3	L↔SbSI	33.3	33.3	33.3	675
4	e_1	L↔Sb+Sb$_2$S$_3$	43	57	-	795
5	e_2	L↔Sb+SbI$_3$	26	-	74	442
6	e_3	L$_1$↔SbI$_3$+I$_2$	12	-	88	353
7	e_4	L↔S+I$_2$	-	80	20	338
8	e_5	L↔SbSI+Sb$_2$S$_3$	35.5	42	22.5	660
9	e_6	L↔SbSI+SbI$_3$	26	2	72	430
10	e_7	L ↔Sb+SbSI	36	32	32	655
11	$e_8{}^*$	L ↔Sb$_2$S$_3$+S	<1	>98	<1	390
12	$e_9{}^*$	L ↔SbSI+S	<1	>98	<1	390
13	$e_{10}{}^*$	L ↔SbI$_3$+S	<1	>98	<1	387
14	E_1	L ↔Sb+SbSI+Sb$_2$S$_3$	37	41	22	650
15	E_2	L ↔Sb+SbSI+SbI$_3$	26.5	1.5	72	428
16	$E_3{}^*$	L ↔Sb$_2$S$_3$+SbSI+S	<1	>98	<1	388
17	$E_4{}^*$	L ↔SbSI+SbI$_3$+S	<1	>98	<1	385
18	E_5	L ↔SbI$_3$+S+I$_2$	1	79	20	335
19	$m_1(m_1{}^/)$	L$_1$↔L$_2$+Sb	95(43)	5(57)	-	892
20	$m_2{}^*(m_2{}^/)$	L$_2$↔L$_3$+Sb$_2$S$_3$	35(2)	65(98)	-	775
21	$m_3(m_3{}^/)$	L$_1$↔L$_2$+Sb	95(30)	-	5(70)	900
22	$m_4(m_4{}^/)$	L$_1$↔L$_2$+Sb	95(38)	2.5(31)	2.5(31)	895
23	$M(M^{/*})$	L$_2$↔L$_3$+Sb$_2$S$_3$+SbSI	23(3)	65(1)	12(96)	630

Conjugate invariant points and their compositions

in- and monovariant equilibria are degenerated and are positioned very close to the elemental sulfur corner of the composition triangle. Table 1 summarizes the types and coordinates of invariant equilibria, including the binary border subsystems.

Three isopleth sections Sb$_{0.5}$I$_{0.5}$-S, Sb-S$_{0.5}$I$_{0.5}$ and Sb$_{0.4}$S$_{0.6}$-I were studied in the general context of liquidus surface in order to determine the character and the correct positions of the invariant and monovariant equilibria on the phase diagram.

The ternary system Sb-Se-I. It was shown that the quasi-binary sections Sb$_2$Se$_3$-SbI$_3$, Sb-SbSeI, SbI$_3$-Se and SbSeI-Se triangulate the Sb-Se-I system, leading to five independent subsystems. The Sb$_2$Se$_3$-

SbI$_3$ and SbI$_3$-Se quasi-binary sections reported already reinvestigated and their phase diagrams were revised with minor corrections.

The liquidus surface of the Sb-Se-I system (Fig. 8) consists of six fields corresponding to primary crystallization of the elemental components and compounds Sb$_2$Se$_3$, SbI$_3$, SbSeI. The system exhibits the broad immiscibility field ($m_1m_3m_2m'_2m'_3m'_1$), which lies within the field of primary crystallization of antimony and overlaps some 90% of its area. This field starts from the boundary Sb-SbI$_3$ sub-system and penetrates into the composition triangle then crosses the Sb-SbSI section and joins with the immiscibility field of the Sb-Sb$_2$S$_3$ sub-section. Apparently from Fig. 8, four quasi-binary section triangulate Sb-Se-I system into five independent sub-systems - Sb-Sb$_2$Se$_3$-SbSeI, Sb-SbI$_3$-SbSeI, SbSeI-SbI$_3$-Se, Sb$_2$Se$_3$-SbSeI-Se and SbI$_3$-Se-I$_2$. The former two of them are characterized by monotectic and eutectic type equilibria while the latter three are found to be invariant eutectic types. Some in- and monovariant equilibria are degenerated nearest elemental selenium and SbI$_3$ corners. Table 2 summarizes the types and coordinates of nonvariant equilibria, including binary border systems.

The isopleth sections Sb-[Se$_{0.5}$I$_{0.5}$] and [Sb$_{0.5}$I$_{0.5}$]-Se (Figs. 9a, b) that pass the stoichiometric composition of SbSeI are found to be partially quasi-binary sections. Sb-SbSeI is quasi-binary part of the Sb-[Se$_{0.5}$I$_{0.5}$]
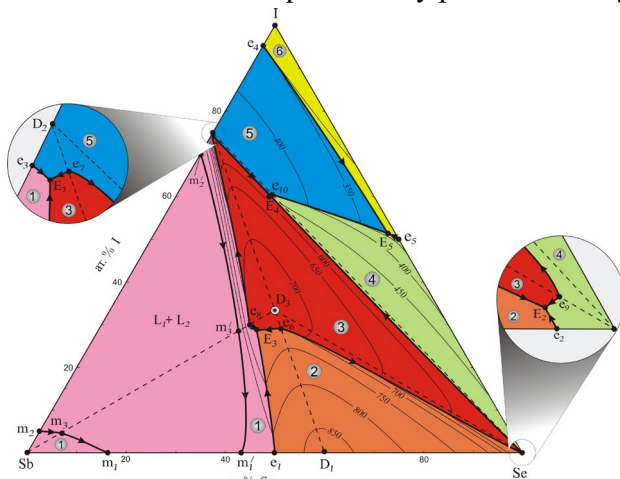
Figure 8. The liquidus surface projection of the Sb-Se-I system (primary crystallization fields 1, Sb; 2, Sb$_2$Se$_3$; 3, SbSeI; 4, Se; 5, SbI$_3$; 6, I$_2$)

Table 2

Invariant equilibria in the Sb-Se-I system

№	Point in Fig. 8	Equilibrium	Composition, mol%		T, K
			Se	I	
1	D_1	L↔Sb_2Se_3	60	-	865
2	D_2	L↔SbI_3	-	75	445
3	D_3	L↔SbSeI	33.3	33.3	725
4	e_1	L↔Sb+Sb_2Se_3	50	-	814
5	e^*_2	L↔Se+Sb_2Se_3	>99	-	493
6	e^*_3	L↔SbI_3+Sb	-	~74	443
7	e_4	L↔SbI_3+I_2	-	88	353
8	e_5	L↔Se+I_2	50	50	330
9	e_6	L↔SbSeI+Sb_2Se_3	38	28	716
10	e^*_7	L↔SbSeI+SbI_3	-	73	443
11	e_8	L ↔Sb+SbSeI	30	30	705
12	e^*_9	L ↔SbSeI+Se	>99	-	492
13	e_{10}	L ↔SbI_3+Se	20	60	435
14	E_1	L ↔Sb+SbSeI+Sb_2Se_3	32	28	698
15	E^*_2	L ↔Sb_2Se_3+SbSeI+Se	>98	-	488
16	E^*_3	L ↔Sb+SbSeI+SbI_3	-	~73	440
17	E_4	L ↔SbSeI+SbI_3+Se	19	59	432
18	E_5	L ↔SbI_3+Se+I_2	46	52	325
19	$m_1(m_1')$	L_1↔L_2+Sb	16(43)	-	853
20	$m_2(m_2')$	L_1↔L_1+Sb_2S_3		5(70)	895
21	$m_3(m_3')$	L_1↔L_2+Sb	5(28)	5(28)	865
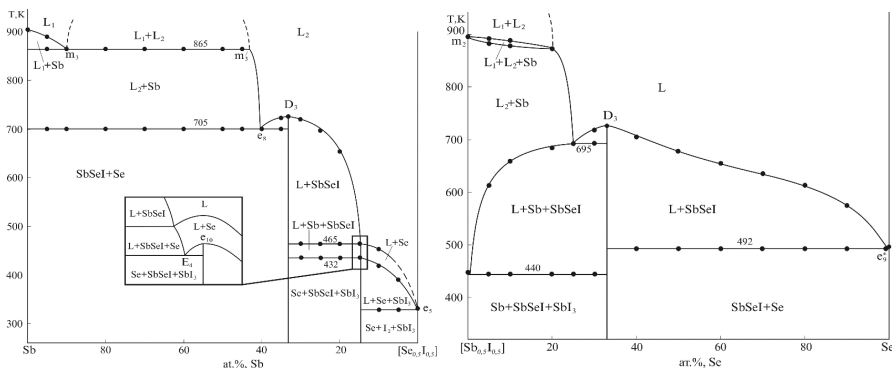
Figure 9. The phase diagram of the (*a*), Sb-[$Se_{0.5}I_{0.5}$] and (*b*), [$Se_{0.5}I_{0.5}$]-Se isopleth

23

Sb-[$Se_{0.5}I_{0.5}$] section. Obviously, it is characterized by the monotectic ($m_3m'_3$, 865 K) and eutectic (e_8, 705 K) equilibria. Within the compositional range of SbSeI-[$Se_{0.5}I_{0.5}$], this section intersects the SbI_3-SbSeI-Se and SbI_3-Se-I sub-systems. The SbSeI-Se part of the [$Sb_{0.5}I_{0.5}$]-Se section exhibits the eutectic type. In the $Sb_{0.5}I_{0.5}$-SbSeI part, this section crosses the Sb-SbI_3-SbSeI sub-system of the Sb-Se-I ternary system. The phase diagram of the isopleth explicitly shows the existence of the L_1+L_2 immiscibility area between 0 and 25 at.% Sb. The third isopleth section $Sb_{0.4}Se_{0.6}$-I that crosses three Sb_2Se_3+SbSeI+Se, SbI_3+SbSeI+Se, SbI_3+Se+I_2 subsystems and enables distinguishing primary crystallization fields of Sb_2Se_3, SbSeI, SbI_3, Se and I_2. Also, it helps to precise the positions of the eutectic curves.

The ternary system Bi-S-I. The phase diagram of the already reported quasi-binary section BiI_3-Bi_2S_3 of this system was confirmed with minor revisions. The phase diagram of the other quasi-binary section BiI_3-S is found to be a simple eutectic type with degenerated eutectic nearest of pure elemental sulfur. The isothermal section of Bi-S-I ternary system at 300K confirms the formation of both ternary
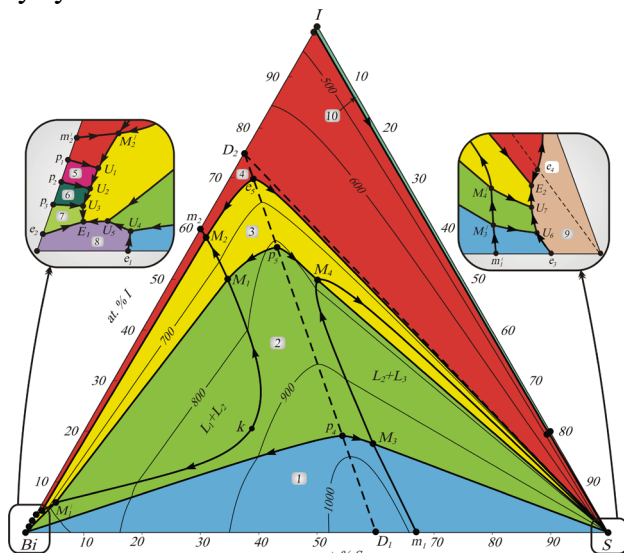
Figure 10. The liquidus surface projection of the Bi-S-I system (primary crystallization fields: 1, Bi_2S_3; 2, BiSI; 3, $Bi_{19}S_{27}I_3$; 4, BiI_3; 5, BiI; 6, Bi_7I_2; 7, Bi_9I_2; 8, Bi; 9, S; 10, I_2

24

Table 3.

Invariant equilibria in the Bi-S-I system

№	Point on Fig. 10	Equilibrium	composition, mol%		T, K
			S	I	
1	D_1	L↔Bi_2S_3	60	-	1048
2	D_2	L↔BiI_3	-	75	681
3	e_1^*	L↔Bi+ Bi_2S_3	99	1	544
4	e_2^*	L↔Bi+ Bi_9I_2	>99	-	542
5	e_3^*	L↔Bi_2S_3+S	>99	-	388
6	e_4^*	L↔BiI_3+S	>98	-	386
7	e_5	L↔BiSI+BiI_3	3.5	70	668
8	e_6	L↔BiI_3+I_2	-	>99	386
9	e_7	L↔S+I_2	80	20	338
10	p_1^*	L+BiI_3↔BiI	-	4	603
11	p_2^*	L+BiI↔Bi_7I_2	-	2.5	573
12	p_3^*	L+Bi_7I_2↔Bi_9I_2	-	2	568
13	p_4	L+Bi_2S_3↔$Bi_{19}S_{27}I_3$	45	19	990
14	p_5	L+$Bi_{19}S_{27}I_3$↔BiSI	15	56.5	808
15	E_1^*	L↔Bi+Bi_9I_2+BiSI	<1	<1	540
16	E_2^*	L↔BiI_3+BiSI+S	>99	<1	383
17	E_3	L↔BiI_3+S+I_2	80	19	337
18	U_1^*	L+BiI_3↔BiI+BiSI	<1	4	600
19	U_2^*	L+BiI↔Bi_7I_2+BiSI	<1	2.5	570
20	U_3^*	L+Bi_7I_2↔Bi_9I_2+BiSI	<1	2	565
21	U_4^*	L+Bi_2I_3↔Bi+$Bi_{19}S_{27}I_3$	<1	<1	542
22	U_5^*	L+$Bi_{19}S_{27}I_3$↔Bi+BiSI	<1	<1	541
23	U_6^*	L+Bi_2I_3↔Bi+$Bi_{19}S_{27}I_3$	>99	<1	386
24	U_7^*	L+$Bi_{19}S_{27}I_3$↔BiSI+S	>99	<1	385
25	$m_1(m_1'^*)$	L_1↔L_2+Bi_2S_3	67 (99)	-	990
26	$m_2(m_2'^*)$	L_1↔L_2+BiI_3	-	60 (5)	625
27	$M_1(M_1')$	L_2+$Bi_{19}S_{27}I_3$↔L_1+BiSI	11 (3)	50 (6)	725
28	$M_2(M_2'^*)$	L_2+BiSI↔L_1+BiI_3	2 (<1)	58 (4)	610
29	$M_3(M_3'^*)$	L_2+Bi_2S_3↔L_3+$Bi_{19}S_{27}I_3$	51 (>99)	17 (<1)	950
30	$M_4(M_4'^*)$	L_2+$Bi_{19}S_{27}I_3$↔L_3+BiSI	25 (>98)	50 (<2)	790

ternary compounds, $Bi_{19}S_{27}I_3$ and BiSI. Ten three-phase equilibria were found in this system at 300 K. It was found that about all phases are in equilibrium with BiI_3 and BiSI meaning that they are playing a key role in the distribution of the phase areas in the subsolidus area. The liquidus surface projection of the system (Fig. 10) consists of ten primary crystallization fields corresponding to the five binary and two ternary compounds and three elemental components. The prima-

ry crystallization fields of the BiI_3, Bi_2S_3, $Bi_{19}S_{27}I_3$, and BiSI are very large and occupy a major part of the total area of the Bi-S-I triangle. From the crystal growth context the liquid surface of the system, bulk single crystals of the BiSI and $Bi_{19}S_{27}I_3$ compounds, can be easily obtained by crystallization from non-stoichiometric melt in a wide range of concentrations thanks to their large primary crystallization fields. Two wide immiscibility fields are observed in this system. The first one (L_1+L_2) starts from the Bi-I system (m_2m_2') and spreads into the $Bi-BiI_3-Bi_2S_3$ subsystem whereas the second one (L_2+L_3) starts from the Bi_2S_3-S subsystem (m_1m_1') and spreads into the Bi_2S_3-BiI_3-S subsystem. The primary crystallization fields of Bi, S, BiI, Bi_7I_2 and Bi_9I_2 as well as some in- and monovariant equilibria are degenerated close to the elemental Bi and S corners. Table 3 summarizes types and coordinates of invariant equilibria. In addition to quasi-binary sections, two intersecting isopleth BiI-S and $Bi-S_{0.5}I_{0.5}$ were studied in order to determine the nature and exact position of the monovariant processes and coordinates of the invariant points.

The ternary system Bi-Se-I. Unlike analogous other ternary chalcohalogenide systems, the phase equilibria in the Bi-Se-I system were studied only on the independent subsystem Bi_2Se_3-BiI_3-Se. The boundary system BiI_3-Se was constructed for the first time based on DTA data and powder XRD measurements. The section is a quasi-binary one and belongs to a simple eutectic type. The eutectic point lies at ~10 mol% BiI_3 and 485 K. The obtained liquidus curve for the BiI_3 has an S-shape form, which is typical for the systems that have a tendency for immiscibility in the liquid state. The liquidus surface of the Bi_2Se_3-BiI_3-Se consists of four fields corresponding to the primary crystallization of the Bi_2Se_3, BiSeI, BiI_3 and elemental selenium (Fig. 11). The primary crystallization fields are bordered by eutectic e_1U, e_2E, e_3E, UE and peritectic pU monovariant equilibrium curves. There is a wide immiscibility field in the system (area mKm') that occupies a considerable part of the liquidus surface of the Bi_2Se_3. It starts from the Bi_2Se_3-Se subsystem (mm') penetrates into the primary crystallization field of the Bi_2Se_3. As can be seen from Fig. 11, the immiscibility field expands forward pU monovariant curve. The types and temperatures of the invariant equilibria in the system are
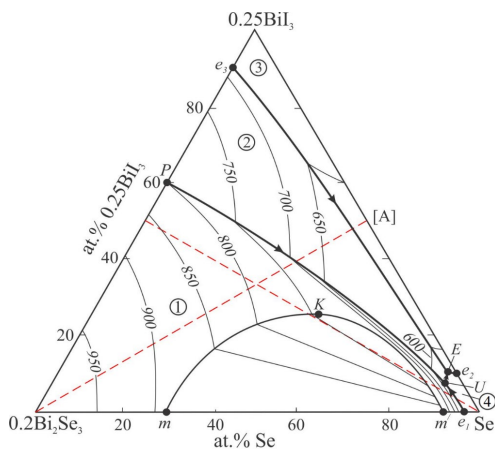
Figure 11. The liquidus surface of the Bi$_2$Se$_3$-BiI$_3$-Se sub-system (primary crystallization fields: 1, Bi$_2$Se$_3$, 2, BiSeI, 3, BiI$_3$, 4, Se)

Invariant equilibria in the Bi$_2$Se$_3$-BiI$_3$-Se sub-system

№	Point on Fig.11	Equilibria	T, K
1	P	L+Bi$_2$Se$_3$↔BiSeI	805
2	$m(m')$	L$_1$↔L$_2$+Bi$_2$Se$_3$	890
3	U	L+Bi$_2$Se$_3$↔BiSeI+Se	487
4	e_1	L↔Bi$_2$Se$_3$+Se	493
5	e_2	L↔BiI$_3$+Se	485
6	e_3	L↔BiSeI+BiI$_3$	665
7	E	L↔BiSeI+BiI$_3$+Se	480

summarized in Table 4. Apparently from Fig. 11 and Table 4, the primary crystallization of the BiSeI compound takes place in a wide concentration range at 805-480 K temperature interval which allows to growth of its bulk single crystals by directional crystallization from melts having non-stoichiometric compositions. The subsystem Bi$_2$Se$_3$-BiI$_3$-Se has no quasi-binary section inside it. Nevertheless, two isopleth sections, BiSeI-3Se and 0.2Bi$_2$Se$_3$-[A] (where component [A] is the heterogeneous mixture Bi$_{0.125}$I$_{0.375}$Se$_{0.5}$ from the BiI$_3$-Se quasi-binary section) were studied in the general context of liquidus surface projection in order to determine the character and the exact positions of the invariant and monovariant equilibrium points and lines on the quasi-ternary phase diagram.

Chapter VI discusses phase equilibria in the reciprocal 3PbSe-Bi$_2$Te$_3 \leftrightarrow$3PbTe-Bi$_2$Se$_3$ and quasi-ternary BiI$_3$-Bi$_2$Se$_3$-BiI$_3$ systems.

Reciprocal system 3PbSe-Bi$_2$Te$_3 \leftrightarrow$3PbTe-Bi$_2$Se$_3$. The isopleth section PbBi$_2$Te$_4$-[PbBi$_2$Se$_4$] of this system is non-quasi-binary (Fig. 12*a*). As can be seen from the phase diagram, the PbSe$_{1-x}$Te$_x$ solid solutions (α-phase) primarily crystallize from the liquid phase. The crystallization process below the liquidus is continuous on the peritectic L+α$\leftrightarrow$γ$_1$ reaction. According to the phase diagram of the PbSe-Bi$_2$Se$_3$ system, an alloy "PbBi$_2$Se$_4$" contains two phases, namely Pb$_5$Bi$_6$Te$_{14}$ and Pb$_5$Bi$_{12}$Te$_{23}$ which are melt incongruently at 993 and 973 K by peritectic reactions L+PbSe$\leftrightarrow$Pb$_5$Bi$_6$Te$_{14}$ and L+Pb$_5$Bi$_6$Te$_{14}\leftrightarrow$Pb$_5$Bi$_{12}$Te$_{23}$ respectively. Taking into account the high probability of forming solid solutions (δ$_1$ and δ$_2$) based on these ternary compounds along the PbBi$_2$Te$_4$-"PbBi$_2$Se$_4$" isopleth, these processes can be written as L+α$\leftrightarrow$δ$_1$ and L+δ$_1\leftrightarrow$δ$_2$. Taking into account these equilibria, one can assume the presence of the following phase areas L+α$\leftrightarrow$δ$_1$, L+δ, L+δ$_1\leftrightarrow$δ$_2$ and δ$_1$+δ$_2$. Horizontal at 935 K on the isopleth section representing an invariant L+δ$_1$+δ$_2\leftrightarrow$γ$_1$ equilibrium. In different finishing versions of this reaction, the following mono-, bi- and triphasic areas can appear in the reciprocal system: γ$_1$, γ$_1$+δ$_1$ (or γ$_1$+δ$_2$) and γ$_1$+δ$_1$+δ$_2$.
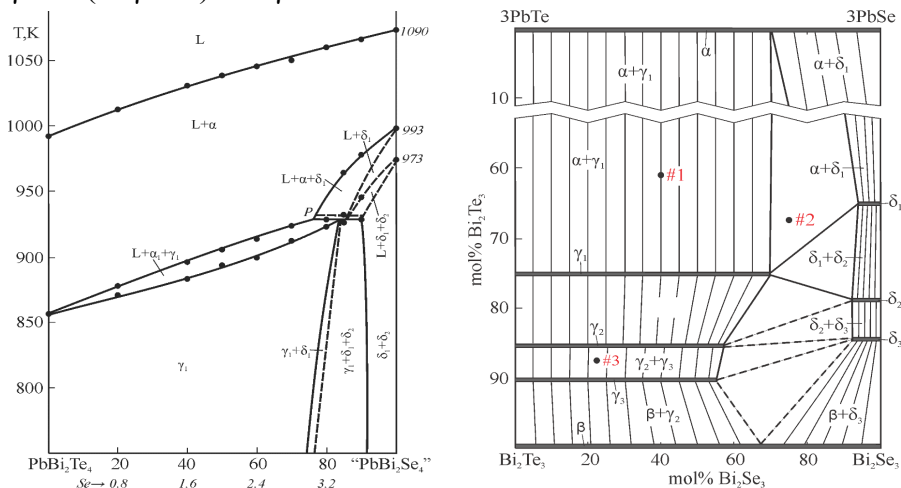
Figure 12. Phase diagram of the (*a*), PbBi$_2$Te$_4$-[PbBi$_2$Se$_4$] isopleth and (*b*), 300 K isothermal of the reciprocal 3PbTe-PbSe-Bi$_2$Se$_3$-3Bi$_2$Te$_3$ system

28

The reciprocal PbTe-PbSe-Bi$_2$Se$_3$-Bi$_2$Te$_3$ system host two types of solid-solutions fields. One of them is the tetradymite-type solid solutions based on the n(PbTe)·m(Bi$_2$Te$_3$) compounds (γ_1, γ_2 and γ_3-phases) in the wide range of concentration, while the second one is the monoclinic structured solid-solutions based on the ternary [(PbSe)$_5$]$_n$[(Bi$_2$Se$_3$)$_3$]$_m$ compounds (δ_1, δ_2 and δ_3-phases) (Fig. 12b). Several bi- and triphasic phase areas appear in the system thanks to these phases. The given phase diagram can shed light on the design of the n(PbTe$_{1-x}$Se$_x$)·m(Bi$_2$Te$_{3-x}$Se$_x$) disordered alloys where tellurium atoms in the quintuple and septuple blocks are substituted by the selenium. The crystal structure of the bulk single crystals of PbBi$_2$Te$_2$Se$_2$, PbBi$_2$Te$_{1.4}$Se$_{2.6}$, PbBi$_4$Te$_4$Se$_3$ and PbBi$_4$Te$_6$Se phases of the system were grown by the Bridgman-Stockbarger method. The crystal structure of the PbBi$_4$Te$_4$Se$_3$ phase from them was elucidated using Rietveld refinement of the powder XRD pattern. Table 5 summarizes its crystal structure parameters, whereas the crystal structure itself is illustrated in Fig. 13. One can see that Se atoms replace entire Te atoms positioned in both sides of the central Pb layer of the 7L block (Te2→Se2 anion substitution in the Te2 positions), and the central Te layer of the 5L block (Te1→Se1 in the Te2 positions).

Table 5.
Crystal structure parameters of the PbBi$_4$Te$_4$Se$_3$ compound

Atom	x	y	
Pb	0	0	0.00000
Bi1	1/3	2/3	0.15847
Bi2	1/3	2/3	0.42031
Te1	0	0	0.23213
Te2	2/3	1/3	0.34613
Se1	0	0	0.50000
Se2	2/3	1/3	0.07406
Space group	a	c	z
$P\text{-}3m1$	4.3224 Å	23.3725 Å	1
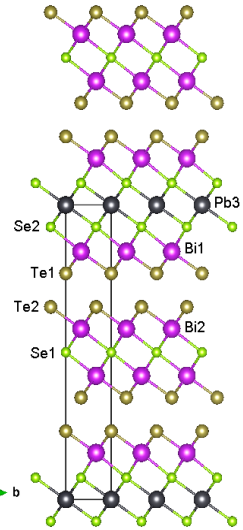
Figure 13. Crystal structure of the PbBi$_4$Te$_4$Se$_3$ compound

Quasi-ternary system BiI₃-Bi₂Se₃-BiI₃. The isothermal section of the system at 300 K (Fig. 14*a*) confirms the existence of the BiI₃, β-(Bi₂Se₃₋ₓTeₓ), γ₁- (BiSeI based) and γ₂-phases (BiTeI based) and formation of four large biphasic and two triphasic (β+γ₁+γ₂ and γ₁+γ₂+BiI₃) areas formed by them. No new quaternary compounds were detected in this system. Four primary crystallization fields were revealed on the liquidus surface projection (Fig. 14*b*) corresponding to the BiI₃, β, γ₁, and γ₂-phases. The crystallization of the β-phase occurs in the largest part of the system and it opens up new opportunities to grow large single crystals of Bi₂Se₃₋ₓTeₓ solid solutions. The crystallization fields of the γ₁ and γ₂-phases are not too small and allow to fabricate bulk single crystals of BiTe₁₋ₓSeₓI solid solutions by crystallization from the melt. The phase diagram relates to an invariant eutectic type, and it features an invariant transition and eutectic equilibria. The isopleth sections BiSeI-BiTeI, BiSeI-Bi₂Te₃, BiTeI-Bi₂Se₃, and [A]-BiTeI (A-Bi₁.₂₅Se₀.₇₅I₂.₂₅) of the BiI₃-Bi₂Se₃-BiI₃ system were studied in the context of the 300 K isothermal and liquidus surface projection. Among them, the study of the BiSeI-BiTeI isopleth is of particular importance in the context of the design of γ₁ and γ₂-phases. The system was found to be non-quasi-binary and represented by the liquidus surface of the β-phase in the wide range of composition (0-75 mol% BiTeI). The primary crystallization of the γ₂-phase based on the BiTeI occurs in the BiTeI-rich part of the system.
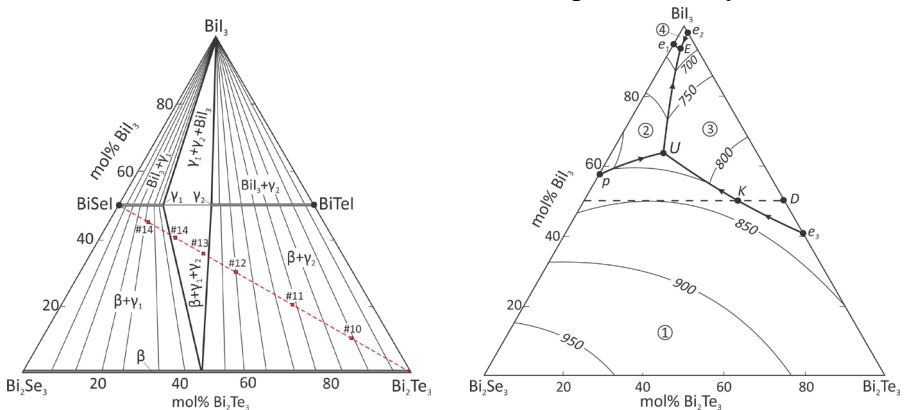
Figure 14. (*a*), 300 K isothermal of the BiI₃-Bi₂Se₃-BiI₃ system and (*b*), liquidus surface projection (1, β; 2, γ₁; 3, γ₂; 4, BiI₃)
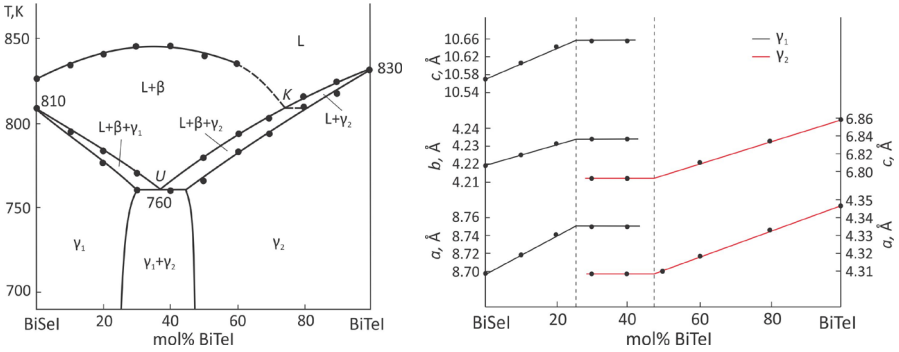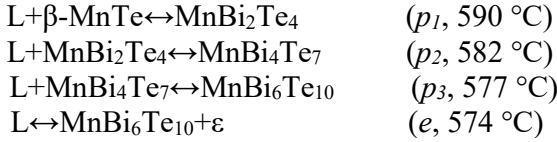
Figure 15. (*a*), phase diagram of the BiSeI-BiTeI isopleth and (*b*), concentration dependence of lattice constants of the BiTe$_{1-x}$Se$_x$I alloys

Crystallization process continues via peritectic reactions L+β↔γ$_1$ and L+β↔γ$_2$ in the concentration ranges of 0-35 mol% and >35 mol% BiTeI, respectively. Consequently, γ$_1$ and γ$_2$-areas were found in the subsolidus areas within the compositional ranges <30 mol% and >45 mol% BiTeI, respectively. From the PXRD patterns, the crystal lattice constants for γ$_1$ and γ$_2$-phases series were calculated. The concentration dependence of the orthorhombic *Pnma* (BiSeI based) and trigonal *P3m*1 (BiTeI based) lattice constants of the BiTe$_{1-x}$Se$_x$I alloys is shown in Fig. 15*b*. Apparently, within the homogeneity region of each phase, the unit cell constants change gradually upon composition, whereas they remain constant in the biphasic area indicating that the system follows Vegard's rule very well. The γ$_1$-phases are expected to have optimized photo- and ferroelectric properties as the well-known BiSeI ferroelectric, whereas the γ$_2$ series can exhibit large Rashba-type spin splitting similar to bulk BiTeI, which is known as a giant Rashba semiconductor.

Chapter VII explores the phase relationships in the Mn-Bi-Te ternary system along the MnTe-Bi$_2$Te$_3$ section in order to search for new van der Waals phases in this system. As can be seen from the phase diagram (Fig. 16) the MnTe-Bi$_2$Te$_3$ system is quasi-binary and hosts three ternary compounds. Apart from previously known MnBi$_2$Te$_4$, there are two new compounds MnBi$_4$Te$_7$ and MnBi$_6$Te$_{10}$. The system is featured by the presence of the following invariant peritectic and eutectic reactions:

$$L+\beta\text{-MnTe}\leftrightarrow MnBi_2Te_4 \qquad (p_1,\ 590\ °C)$$
$$L+MnBi_2Te_4\leftrightarrow MnBi_4Te_7 \qquad (p_2,\ 582\ °C)$$
$$L+MnBi_4Te_7\leftrightarrow MnBi_6Te_{10} \qquad (p_3,\ 577\ °C)$$
$$L\leftrightarrow MnBi_6Te_{10}+\varepsilon \qquad (e,\ 574\ °C)$$

The heterogeneous mixtures of the αMnTe, $MnBi_2Te_4$, $MnBi_4Te_7$, and $MnBi_6Te_{10}$ were observed in the $MnBi_2Te_4$, $MnBi_4Te_7$, and $MnBi_6Te_{10}$ ingots due to the peritectic reactions have close temperatures and narrow primary crystallization fields. The crystal structure of the $MnBi_4Te_7$ and $MnBi_6Te_{10}$ phases was refined by the Rietveld method using the XRD pattern of the ingot having the starting composition $MnBi_4Te_7$ (Fig. 17, Table 6 and 7). As the refinement was performed using the multiphase mixture, several parameters were constrained to avoid excessive correlations; in particular, all atomic displacement parameters were restrained to be equal for each crystal structure and no mixing of Mn/Bi was allowed. The crystal structures of $MnBi_4Te_7$ and $MnBi_6Te_{10}$ can be regarded as the intergrowth structures; together with the crystal structures of $MnBi_2Te_4$ and Bi_2Te_3, they can be expressed by the following sequence of the 5L and 7L blocks: $MnBi_2Te_4$ -7-7-7-, $MnBi_4Te_7$ -5-7-5-7-, $MnBi_6Te_{10}$ -5-5-7-5-5-7-, and Bi_2Te_3 -5-5-5-. Raman characteristics of $(MnTe)\cdot n(Bi_2Te_3)$ compounds were measured on the obtained single crystals. Raman spectra of the studied crystals along with the common features such
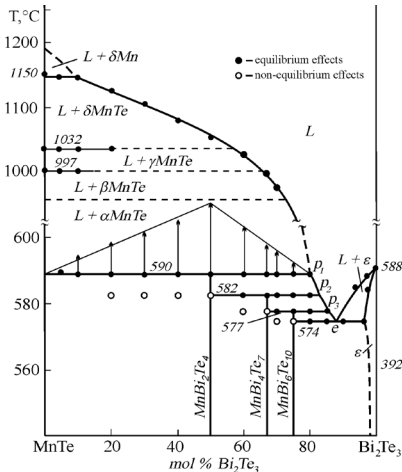
Figure 16. Phase diagram of the quasi-binary MnTe-Bi$_2$Te$_3$ system
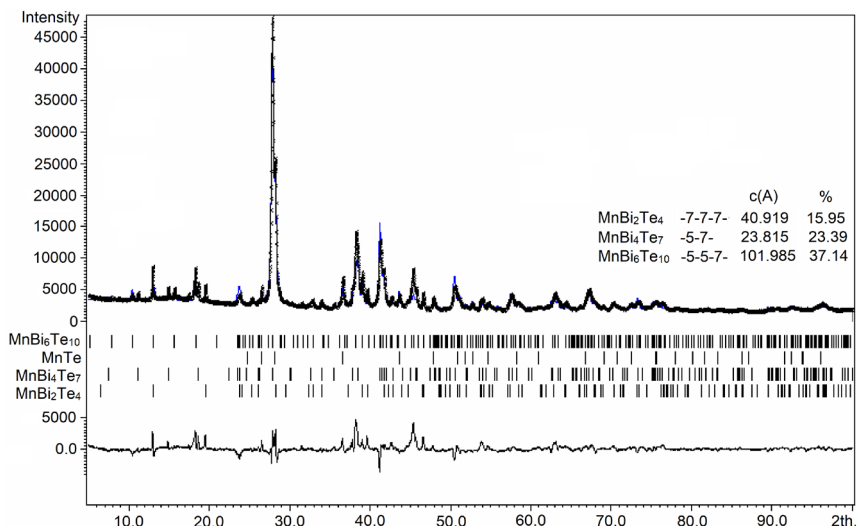
Figure 17. Rietveld fitted pattern of the MnBi4Te7 ingot

In the figure legend:

		c(A)	%
$MnBi_2Te_4$	-7-7-7-	40.919	15.95
$MnBi_4Te_7$	-5-7-	23.815	23.39
$MnBi_6Te_{10}$	-5-5-7-	101.985	37.14

Crystal structure data and details of data refinement for the
$(MnTe) \cdot n(Bi_2Te_3)$ compounds

	$MnBi_2Te_4$	$MnBi_4Te_7$	$MnBi_6Te_{10}$	MnTe
Space group	*R-3m*	*P-3m*1	R-3m	*P6₃/mmc*
Z	3	1	3	2
Temperature (K)	293	293	293	293
Unit cell: a (Å)	4.3304(4)	4.355(1)	4.3745(3)	4.1498(4)
c (Å)	40.919(4)	23.815(1)	101.985(8)	6.7176(7)
Unite volume (Å³)	664.5(1)	391.3(2)	1690.2(2)	100.18(2)
Density (g/cm³)	7.54(9)	6.93(4)	7.74(4)	6.051(1)
2θ range	5÷120°	5÷120°	5÷120°	5÷120°
$R_{hkl\text{-Lebail fitting}}$(%)	0.344	0.064	0.326	0.216
R_{Bragg} (%)	3.91	3.23	4.39	3.02

as the similar number of lines and similar spectral range, are charac-terized by different line positions. Characteristic frequencies of the Raman-active modes of the same type in the studied materials differ from each other, depending on the nominal chemical composition. Therefore, we can conclude that not only samples of $MnBi_2Te_4$ but also the samples of the other two materials are very likely to reflect the chemical composition indicated by the phase diagram; i.e. their chemical compositions of the latter are $MnBi_4Te_7$ and $MnBi_6Te_{10}$.

Table 7

Atomic coordinates and displacement parameters for the crystal structures of $(MnTe) \cdot n(Bi_2Te_3)$ compounds

Atom	Wyckoff	x/a	y/b		z/c	B
			$MnBi_2Te_4$			
Bi1	6c	0	0		0.42539(12)	1.17(2)
Te1	6c	0	0		0.13364(19)	1.17(2)
Te2	6c	0	0		0.2953(2)	1.17(2)
Mn1	3a	0	0		0	1.17(2)
			$MnBi_4Te_7$			
Bi1	2d	1/3	2/3		0.0842(3)	0.50(2)
Bi2	2d	1/3	2/3		0.3446(3)	0.50(2)
Te1	1a	0	0		0	0.50(2)
Te2	2d	2/3		1/3	0.1557(6)	0.50(2)
Te3	2c	0	0		0.2645(6)	0.50(2)
Te4	2d	2/3	1/3		0.4355(4)	0.50(2)
Mn1	1b	0	0		1/2	0.50(2)
			$MnBi_6Te_{10}$			
Bi1	6c	0	0		0.23668(8)	3.00(11)
Bi2	6c	0	0		0.29571(7)	3.00(11)
Bi3	6c	0	0		0.4702(17)	3.00(11)
Te1	6c	0	0		0.05364(13)	3.00(11)
Te2	6c	0	0		0.11732(18)	3.00(11)
Te3	6c	0	0		0.17912(15)	3.00(11)
Te4	6c	0	0		0.34919(12)	3.00(11)
Te5	6c	0	0		0.41446(17)	3.00(11)
Mn1	3a	0	0		0	3.00(11)

Chapter VIII provides the justification of the role of phase diagrams in the development of methods for single crystals growth of chalcogenide and chalcohalogenide phases having TI, TE and Rashba semiconductor properties. The information stored in the phase diagram is especially important for the growth of single crystals of different phases from melts with different versions of directional crystallization, or for the development of scientific and technological bases for the direct synthesis of those phases. In order to explain the role of phase diagrams in single crystal growth, the phase diagrams of model quasi-binary systems with different crystallization or phase formation characteristics, forming stable and variable intermediate compounds, and synthesis methods for the phases with different for-

mation characteristics are considered. In addition, the elaboration of single crystals of binary tellurides by the Bridgman-Stockbarger method has been discussed in the general context of the phase diagrams of the real A^V-Se and A^V-Te systems.

The single crystals growth problems of the ternary tellurides of the phase diagrams of Ge(Pb)Te-Bi$_2$Te$_3$ systems are considered. Phase diagrams are an important source for determining optimal parameters of the single crystal growth process and in many cases require reinvestigation due to some inconsistencies or contradictions. According to the known phase diagrams of both systems, their ternary compounds are formed by peritectic reactions in a very small temperature range. Therefore, the synthesis and crystal growth process of these phases are quite difficult. Taking into account these problems and actuality, after the refinements made on GeTe-Bi$_2$Te$_3$ and PbTe-Bi$_2$Te$_3$ systems, the high-quality single crystals of the GeBi$_2$Te$_4$, GeBi$_4$Te$_7$, PbBi$_2$Te$_4$, PbBi$_4$Te$_7$ and PbBi$_6$Te$_{10}$ compounds were obtained by the Bridgman-Stockbarger method in order to further study their surface physical and chemical properties. A single crystalline ingot of the PbBi$_6$Te$_{10}$ phase was grown using the revised version of the PbTe-Bi$_2$Te$_3$ system. According to the crystallization sequence of the phases found on the phase diagram, the ingot was found to be consist of PbBi$_4$Te$_7$ at the bottom and PbBi$_6$Te$_{10}$+PbBi$_8$Te$_{13}$ mixture at the middle and top parts.

Thus, using the phase diagrams, more than 60 high-quality single-crystals of pure and doped phases were grown and used to further study numerous physical and chemical properties.

Chapter IX discusses an investigation of some mechanical properties and surface chemical activity of some single-crystalline bismuth chalcogenides having TI properties to determine their application fields and conditions.

An examination of the surface chemical reactivity of some binary and ternary bismuth chalcogenides.

In this work, we report X-ray photoemission spectroscopy investigation with synchrotron radiation on the chemical reactivity of: (1) Bi$_2$Se$_3$ toward oxygen in the 300-550 K temperature range; (2) Bi$_2$Se$_3$ toward the water at room temperature; (3) Bi$_2$Se$_3$, Bi$_2$Te$_3$, GeBi$_2$Te$_4$,

and $PbBi_6Te_{10}$ toward carbon monoxide at room temperature.

Fig. 18*a* and *b* (upper panel) display effects of a prolonged, 10^5 Langmuir O_2 (1 Lanqmuir=10^{-6} torr·s) exposure at room temperature on *4f*-Bi, *3p*-Se and *3d*-Se core level electrons. As can be seen, no any change with respect to the pristine Bi_2Se_3 is noticeable meaning that it is completely inert toward oxygen in the temperature range from 300 up to 550 K. Fig. 18*c* and *e* (bottom panel) show XPS spectrums of $SnBi_4Te_7$ acquired after dosing 1000 L of O_2 at the 300 K. Apparently, only *3d*-Te ($3d_{3/2}$ and $3d_{5/2}$) *3d*-Sn ($3d_{3/2}$ and $3d_{5/2}$) and *4f*-Bi ($4f_{5/2}$ and $4f_{7/2}$) core levels are visible on both cases. Consequently, given XPS spectrums are identical meaning the $SnBi_4Te_7$ is robust toward oxygen. ARPES spectrum of the $SnBi_4Te_7$ after O_2 exposure proves that both Dirac states of this compound remain well protected. No vanishing of electronic states, energy shifts, or new extra electronic states was observed indicates that the Dirac state of the $SnBi_4Te_7$ is very robust against oxygen exposure.

The Bi_2Se_3 sample has been exposed to 1000 L of water at room temperature. The top spectrum of Fig. 19 shows the presence of a *1s*-O peak, indicating that water interacts with Bi_2Se_3.

Fig. 19 shows the wide XPS spectra of Bi_2Se_3, Bi_2Te_3 and $GeBi_2Te_4$ single crystals exposed to 50 L of CO at room temperature.
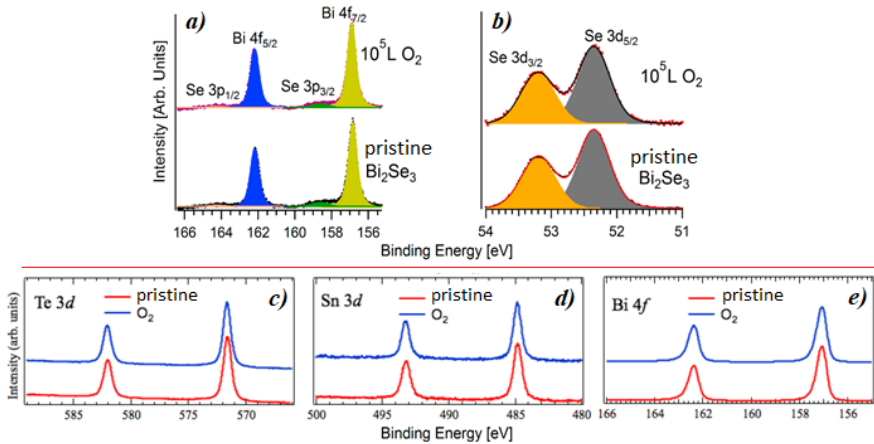
Figure 18. (upper panel) (*a*) *4f*-Bi and *3p*-Se core levels; (*b*) *3d*-Se core levels after 10^5 L O_2 exposure at 300 K, (bottom panel) (*c*) *3d*-Te, (*d*) *3d*-Sn, and (*e*) *4f*-Bi core levels of $SnBi_4Te_7$ after dosing 1000 L O_2 at 300 K
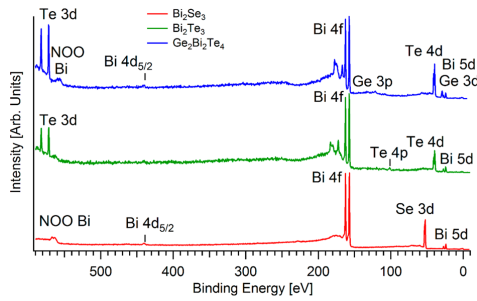
Figure 19. XPS spectrum of Bi_2Se_3, Bi_2Te_3 and $GeBi_2Te_4$ after exposure to 50 L of CO.

No features arising from C or O are noticeable in photoemission spectra meaning that carbon monoxide does not interact with these materials. However, different results have been obtained by exposing the ternary compound $PbBi_6Te_{10}$ to CO. The presence of both $1s$-O and $1s$-C core levels in XPS spectra indicates that this single crystal-line material reacts toward CO.

Mechanical properties of the single-crystal TI Bi_2Te_3. The mechanical properties of the single-crystalline Bi_2Te_3 i.e., fracture toughness (K_c), hardness (H), and Young's modulus (E_r) were not reported so far. The depth-sensing nanoindentation method is the best choice to determine these properties. Here, the dimensions of the indenter trace on the surface of the sample and the values of the load applied to the indenter are combined to determine the along with the H and E_r coefficient of the material. To date, several models have been developed to determine the K_c coefficient of the brittle materials by this method. Among them, the model proposed by Dukino and Swain, which can be considered as an extension of Laugier's model using a Berkovich tip is the most universal one:

$$K_c = 1.073 x_v \left(\frac{a}{l}\right)^{1/2} \left(\frac{E}{H}\right)^{2/3} \frac{P}{c^{3/2}}$$

For fracture toughness determination, a set of 30 nanoindentations with increasing loads were performed. The maximum load varied between 1 and 30 mN with increments of 1 mN. A stable value for K_c was obtained by Dukino and Swain model in the $13 \div 30$ mN range. The fracture toughness of Bi_2Te_3 bulk single-crystal was then determined to be 0.042 ± 0.016 MPa. It is concluded that the low values of

fracture toughness of Bi_2Te_3 bulk single crystals could limit the use of this topological insulator in flexible microelectronics or nanoelectromechanical devices, in contrast with the results obtained with black phosphorus, graphene, and MoS_2. Nanoindentation measurements allow determining Young's modulus and hardness along with fracture toughness. The E_r and H values were obtained from load-penetration depth curves, according to the model proposed by Oliver and Pharr. Fig. 20 displays the distribution of reduced E_r and material hardness as a function of the penetration depth of the nanoindenter. As can be seen, at the beginning (≤ 40 nm) there is a significant increase in both parameters as the penetration depth of the indenter increases, and in the range $h=40 \div 200$ nm there is a decrease towards stable values. The initial increase was ascribed to the transition from elastic to elasto-plastic contact conditions, whereas the subsequent decrease was related to the establishment of fully plastic contact. The results of five consecutive tests were averaged after the establishment of fully plastic contact conditions ($h \approx 100$ nm). The reduced Young's modulus and the hardness were found to lie in the range $E_r=32.4\pm2.9$ GPa and $H=1.6\pm0.2$ GPa, respectively. Apparently from Fig. 20, these values can be reasonably assumed to be intrinsic material properties of the single crystal within the depth range ~100-400 nm.
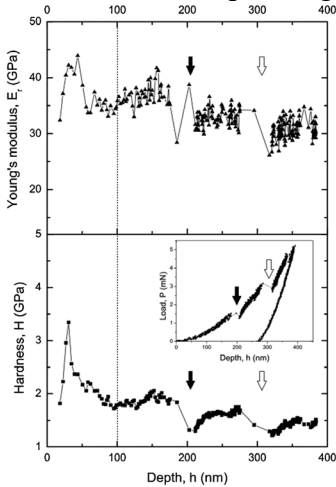
Figure 20. Young's modulus (*a*) and material hardness (*b*) as a function of the penetration depth

38

X Chapter briefly discusses the results regarding the surface and bulk electronic properties of the numerous trivial and magnetic 3D TIs and, manipulating of these properties by doping or hybrid interfaces creation with organic or metal-organic molecules. These works were done in collaboration with the world-known research groups (under the supervision of prof. E. V. Chulkov from Basque Country University and Donostia International Physics Center). According to these results, the potential application fields are shown.

The electronic band structure of the $PbBi_4Te_7$ and $PbBi_6Te_{10}$ from $n(PbTe) \cdot m(Bi_2Te_3)$ homologous series was studied. It was found that in $PbBi_4Te_7$, the Dirac state is buried about 10-25 Å under the 5L-terminated surface or in the topmost 7L block which makes this state more protected against possible surface modifications. Both in the $PbBi_4Te_7$ and $PbBi_6Te_{10}$ revealed coexisting topological and multiple Rashba-like split states close to the Fermi level. The observed topological states derive from different surface terminations which are typical for both compounds.

The electronic properties and spin structure of the $PbBi_2Te_2Se_2$ and $PbBi_2Te_{1.4}Se_{2.6}$ phases from the $PbBi_2Te_{4-x}Se_x$ series were studied. Both the phases are found to be characterized by a spin-polarized TSS in the bulk gap and, revealed that increasing Se content leads to the increase of the band gap up to 300 meV, which is three times larger than the value for the pristine $PbBi_2Te_4$ (90 meV) compound. The electronic band structure of the $PbBi_4Te_4Se_3$ for both 5L and 7L surface terminations is investigated. The bulk band-gap of this phase is found to be about 300 meV which is notably larger than $PbBi_4Te_7$ (100 meV).

SARPES and ARPES study shows that the size of the bulk energy gap for $GeBi_2Te_4$ is determined to be ~180 meV, and TSS below and above the Dirac point are found to be isolated from the bulk band.

Time-resolved two-photon photoemission was used to study the electronic structure and dynamics at the surface of $SnSb_2Te_4$. The Dirac point is found 0.32 ± 0.03 eV above the Fermi level. Electrons from the conduction band minimum are scattered on a time scale of 43 ± 4 fs to the Dirac cone and from there they decay to the partly depleted valence band in 78 ± 5 fs.

In order to optimization of electronic surface properties (TSS) of the B_2Se_3, its surface is manipulated with carbon, cesium, organic and metal-organic molecules. Surface X-ray Diffraction experiments revealed that carbon atoms penetrate inside the topmost 5L of Bi_2Se_3 and induce an expansion of ≈11%. It was also observed an upward shift of the DP by 40±20 meV.

We studied the electronic structure modification induced by the adsorption of different coverage of cobalt phthalocyanine on the Bi_2Se_3 surface. ARPES results point toward the existence of relevant interaction between the molecule and the surface underneath, with the effect of burying the wave function of the TSS below the first 5L. Thus, it has been established that the TSS and the Dirac point within the Fermi level of the layered TIs can be controlled by the dopants.

Plasmonic excitations at the surface of Sb_2Te_3 and Bi_2Se_3 single crystals were studied, and it was found that both crystals had linear and parabolic dispersions for both low- and high-energy plasmons. In order to study the potential application of plasmon excitations of TIs surface surfaces in real devices, activation, probing, and exploitation of the collective electronic excitation of TSS in the Dirac cone of Bi_2Se_3 were explored. Using the obtained data, a laboratory prototype of the first room-temperature terahertz detector was designed.

$MnBi_2Te_4$ compound of the Mn-Bi-Te system is found to be an interlayer antiferromagnet, in which ferromagnetic Mn layers are coupled antiparallel to each other and the easy axis of staggered magnetization is perpendicular to the layers, consequently, confirm that the $MnBi_2Te_4$ is the first-ever observed antiferromagnetic topological insulator (AFMTI)

We also report new $(MnBi_2Te_4)\cdot n(Bi_2Te_3)$ homologous series of the van der Waals compounds, namely $MnBi_4Te_7$ ($n=1$) and $MnBi_6Te_{10}$ ($n=2$) as intrinsic magnetic TIs. Magnetic and electronic, consequently, topological properties of these materials depend strongly on the n value and are thus highly tunable. The antiferromagnetic coupling between the neighboring Mn layers strongly weakens on moving from $MnBi_2Te_4$ ($n=0$) to $MnBi_4Te_7$ ($n=1$) and $MnBi_6Te_{10}$ ($n=2$). For $MnBi_4Te_7$, there is a strong weakening of the interlayer AFM coupling due to the insertion of the non-magnetic 5L block between neighboring 7L. Increasing by one the number of 5L between 7L and forming $MnBi_6Te_{10}$ leads to further weakening of the interlayer exchange interaction.

CONCLUSION

1. To search and design new multifunctional materials having trivial and magnetic TI, TE, Rashba spin splitting, and photovoltaic-ferroelectric properties, ternary Yb-Sb(Bi)-Te, Sb-S(Se)-I, Bi-S(Se)-I, Mn-Bi-Te and quaternary $YbTe-Sb_2Te_3-Bi_2Te_3$, $YbTe-SnTe-Sb_2Te_3(Bi_2Te_3)$, $Bi_2Se_3-Bi_2Te_3-BiI_3$ and $3PbSe-Bi_2Te_3\leftrightarrow3PbTe-Bi_2Se_3$ systems were investigated, the phase diagrams of their isopleth and isothermal sections, liquidus surface projections were plotted. The primary crystallization and homogeneity areas, as well as types and coordinates of the in- and monovariant equilibria, were determined:

– The earlier reported ternary $YbSb_2Te_4$, $YbSb_4Te_7$, $YbBi_2Te_4$, and $YbBi_4Te_7$ compounds were not confirmed in the quasi-ternary $YbTe-Sb_2Te_3-Te$, $YbTe-Bi_2Te_3-Te$, and $YbTe-Sb_2Te_3-Bi_2Te_3$ systems. Wide solid solutions areas based on starting Sb_2Te_3 and Bi_2Te_3 phases were revealed in all three systems.

– The $YbSnTe_2$ compound reported earlier in the YbTe-SnTe quasi-binary system was not confirmed within the $YbTe-SnTe-Sb_2Te_3$ and $YbTe-SnTe-Bi_2Te_3$ quasi-ternary systems. Instead, the continuous solid solution series was revealed and found that a spinodal-type phase decomposition of this solid solution occurs below ~950 K.

– The existence of the SbSI, SbSeI, BiSI, $Bi_{19}S_{27}I_3$, and BiSeI compounds in the ternary Sb-S(Se)-I, Bi-S(Se)-I systems were confirmed, their primary crystallization, homogeneity, and heterogeneous phase areas are determined.

– Two wide Te↔Se substituted solid-solution series were synthesized in the $Bi_2Se_3-Bi_2Te_3-BiI_3$ quasi-ternary system along the BiSeI-BiTeI section.

– Within the $3PbSe-Bi_2Te_3\leftrightarrow3PbTe-Bi_2Se_3$ reciprocal system, Te→Se substituted solid-solutions based on $PbBi_2Te_4$, $PbBi_4Te_7$, $PbBi_6Te_{10}$ compounds and Se→Te substituted solid-solution series based on $Pb_5Bi_6Se_{14}$, $Pb_5Bi_{12}Se_{23}$ and $Pb_5Bi_{18}Se_{32}$ compounds were synthesized.

– New members of the $(MnTe)\cdot n(Bi_2Te_3)$ homologous series - $MnBi_4Te_7$ and $MnBi_6Te_{10}$ van der Vaals compounds were discovered in the quasi-binary $MnTe-Bi_2Te_3$ section of the Mn-Bi-Te system.

2. The synthesis and crystal growth methods of the newly revealed phases were developed and realized based on plotted phase diagrams. The synthesis and thermal annealing regimes for the synthesis of polycrystalline samples, starting compositions of the liquid phases and temperatures of the furnace zones for the single crystal growth process were chosen from respective phase diagrams. The known phase diagrams of the binary Sb-Te, Bi-Se(Te) and some ternary A^{IV}-A^{V}-Te systems were critically reinvestigated in the context of crystal growth problems. As a result, single crystals of their intermediate phases were grown either by the Bridgman-Stockbarger method or by chemical vapor transport methods.

3. The crystal structure parameters of the novel compounds and solid-solution phases were determined by XRD measurements. The XRD patterns of some phases were analyzed by the Rietveld method and consequently, crystal structures were elucidated or refined.

4. Crystal structure of the new manganese bismuth tellurides were determined by the Rietveld method, their Raman characteristics were done at room temperature. $MnBi_2Te_4$ has been identified as the first antiferromagnetic topological insulator which is a new quantum state of matter. The other two compounds in this system are also found to be magnetic topological insulators. The antiferromagnetic coupling between the neighboring Mn layers strongly weakens on moving from $MnBi_2Te_4$ ($n=0$) to $MnBi_4Te_7$ ($n=1$) and $MnBi_6Te_{10}$ ($n=2$).

5. Surface and bulk electronic properties of the single crystalline $PbBi_4Te_7$, $PbBi_6Te_{10}$ $SnBi_2Te_4$, $SnBi_4Te_7$, $GeBi_2Te_4$ compounds from $n(A^{IV}Te) \cdot m(Bi_2Te_3)$ homologous series were studied in an international collaboration with world-known research groups. The electronic properties of the Bi_2Se_3 can be tuned via the doping or creation of hybrid interfaces with organic or metal-organic molecules. Plasmonic excitations on the surface of Sb_2Te_3 and Bi_2Se_3 were studied and a laboratory prototype of the first room-temperature terahertz detector based on Bi_2Se_3 surface plasmonic excitations was designed.

6. To study the effect of Te→Se substitution on the electronic properties of $PbBi_2Te_4$ and $PbBi_4Te_7$ compounds, single crystals of the $PbBi_2Te_2Se_2$, $PbBi_2Te_{1.4}Se_{2.6}$, $PbBi_4Te_4Se_3$ and $PbBi_4Te_6Se$ phases of the $PbBi_2Te_{4-x}Se_x$ and $PbBi_4Te_{7-x}Se_x$ solid solution series were grown.

Their crystallographic, electronic, and spin properties were studied. The crystal structure of $PbBi_4Te_4Se_3$ phase was revealed by Rietveld refinement and found that there are Te2→Se2 and Te1→Se1 substitutions in the 7L and 5L blocks of -5-7- type structure, respectively. It was also found that increasing Se content in both the $PbBi_2Te_{4-x}Se_x$ and $PbBi_4Te_{7-x}Se_x$ solid solutions leads to the increase of the band gap three times larger than the value of the pristine compounds.

7. The surface chemical robustness of the single-crystalline binary and ternary bismuth chalcogenides against O_2, H_2O, and CO were studied. It was found that the surface layers of the Bi_2Se_3 are inert against O_2 at 300-550 K intervals, however, it reacts toward the water. $SnBi_4Te_7$ surface layers are found to be quite inert toward O_2. The chemical inertness of Bi_2Se_3, Bi_2Te_3, $GeBi_2Te_4$, and $PbBi_6Te_{10}$ single crystalline layers against CO were studied and found that the former three compounds are inert to CO exposure while it reacts positively to the latter compound $PbBi_6Te_{10}$.

8. The fracture toughness of the Bi_2Te_3 single crystal was measured using Berkovich nanoindenter and the model proposed by Dukino and Swain. Nanoindentation measurements allow determining the fracture toughness of material (K_c=0.042±0.016 MPa), together with Young's modulus (E_r=32.4±2.9 GPa) and hardness (H=1.6±0.2 GPa.) from load-penetration depth curves, according to the model proposed by Oliver and Pharr.

List of published works

1. M. B. Babanly, J. C. Tedenac, Z. S. Aliyev, D. V. Balitsky, Phase equilibriums and thermodynamic properties of the system Bi-TeI, J. Alloys Compd. 481, 2009, p. 349-353.
2. M. B. Babanly, Z. S. Aliev, S. S. Musaeva, Y. M. Shikhiyev, Phase diagram and thermodynamic properties of the B^V-S-I (B^V-As, Sb, Bi) systems, Proceed. Int. conf. HighMatTech-2009, Kyiv, Ukraine, 2009, p. 85
3. Z. S. Aliev, S. S. Musaeva, D. M. Babanly, A. V. Shevelkov, M. B. Babanly: Phase diagram of the Sb-Se-I system and thermodynamic properties of SbSeI, J. Alloys Compd. 505, 2010, p. 450-455.
4. M. B. Babanly, Z. S. Aliev, K. D. Rasulova, G. I. Ibadova, F. M. Sadigov, Physicochemical investigation of the YbTe-Sb_2Te_3-Te system, IX Int. Kurnakov meeting on physicochemical analysis. Perm, Russia, July 5-9, 2010, p. 133
5. S. S. Musaeva, D. M. Babanly, Z. S. Aliev, M. B. Babanly, Quasi-binary section and congruent triangulation of the Sb-Se-I system, IX Int. Kurnakov meeting on physicochemical analysis. Perm, Russia, July 5-9, 2010, p. 224
6. Z. S. Aliyev, J.-C. Tedenac, M. B. Babanly, K. D. Rasulova, G. I. Ibadova, New non-stoichiometric phases in the ternary system Yb-Sb-Te, 8th int. conf. on electronic process in organic and inorganic materials, Ivano-Frankovsk, Ukraine, May17-22, 2010. p. 116-117.
7. S. S. Musaeva, Z. S. Aliyev, K. D. Rasulova, M. B. Babanly, Phase equilibria in the Sb_2Se_3-SbSeI-Se system, News of BSU, series of natural sciences, №2, 2010, p. 24-27.
8. S. S. Musaeva, Z. S. Aliyev, Z. I. Ismailov, M. B. Babanly, Phase equilibria in the Sb-Sb_2Se_3-SbSeI system, Az. Chem J. 2010, №3, p. 71-75
9. M. B. Babanly, S. S. Musaeva, Z. S. Aliyev, The phase diagram of the SbI_3-SbSeI-Se system, Az. Chem. J. №4, 2010, p.141-44
10. Z. S. Aliev, G. I. Ibadova, J. C. Tedenac, A. V. Shevelkov, M. B. Babanly, Solubility of YbTe in Sb_2Te_3 and thermodynamic properties of the solid solution, J. Alloys Compd. 509, 2011, p. 6773-6776
11. Z. S. Aliev, D. M. Babanly, S. S. Musayeva, M. B. Babanly, Phase diagram of the Bi-Se-I system and thermodynamic properties of the BiSeI compound, XVIII Ukraine conf. on inorganic chemistry,

Kharkiv, Ukraine, 2011, p. 218

12. M. B. Babanly, Z. S. Aliev, K. D. Rasulova, G. I. Ibadova, New phases of variable composition in the Yb-Sn(Pb)-Bi-Te systems, II Int. sci.-tech. conf. "functional and construction materials", Donetsk, Ukraine, 2011, p. 20

13. S. V. Eremeev, G. Landolt, T. V. Menshchikova, B. Slomski, Y. M. Koroteev, Z. S. Aliev, M. B. Babanly, J. Henk, A. Ernst, L. Patthey, A. Eich, A. A. Khajetoorians, J. Hagemeister, O. Pietzsch, J. Wiebe, R. Wiesendanger, P. M. Echenique, S. S. Tsirkin, I. R. Amiraslanov, J. H. Dil, E. V. Chulkov, Atom-specific spin mapping and buried topological states in a homological series of topological insulators, Nat. Commun. 3, 2012, p. 635.

14. Z. S. Aliev, M. B. Babanly, A. V. Shevelkov, D. M. Babanly, J.-C. Tedenac, Phase diagram and thermodynamic properties of the system Sb-Te-I, Int. J. Mat. Res. 3, 2012, p. 290-295.

15. G. Landolt, S. V. Eremeev, Y. M. Koroteev, B. Slomski, S. Muff, T. Neupert, M. Kobayashi, V. N. Strocov, T. Schmitt, Z. S. Aliev, M. B. Babanly, I. R. Amiraslanov, E. V. Chulkov, J. Osterwalder, J. H. Dil, Disentanglement of surface and bulk Rashba spin splittings in non-centrosymmetric BiTeI, Phys. Rev. Lett. 109, 2012, p. 116403.

16. K. Okamoto, K. Kuroda, H. Miyahara, K. Miyamoto, T. Okuda, Z. S. Aliev, M. B. Babanly, I. R. Amiraslanov, K. Shimada, H. Namatame, M. Taniguchi, D. A. Samorokov, T. V. Menshchikova, E. V. Chulkov, A. Kimura, Observation of a highly spin-polarized topological surface state in $GeBi_2Te_4$, Phys. Rev. B, 86, 2012, p.195304.

17. M. B. Babanly, G. I. Ibadova, Z. S. Aliev, S. Z. Imamalieva, Solid-phase equilibria in the system $YbTe-SnTe-Sb_2Te_3$, All-Russ. conf. "solid-state chemistry and functional materials", Ekaterinburg, Russia, 2012, c. 7

18. Z. S. Aliev, K. D. Rasulov, S. Z. Imamalieva, J.-C. Tedenac, M. B. Babanly, Physicochemical investigation of systems $YbTe-SnTe(PbTe)-Bi_2Te_3$, XIV int. sci.- tech. conf. "high-tech chemical technologies-2012", Tula-Yasnaya Polyana-Kulikovo Pole, Russia, 2012, p. 270

19. M. B. Babanly, G. I. Ibadova, Z. S. Aliev, S. Z. Imamalieva, Physicochemical investigation of systems $YbTe-SnTe-Sb_2Te_3$, Proceed. of VI All-Russ. conf. "Physicochemical processes in condensed matters

and interphases", Voronezh, Russia, 2012, p. 296

20. Z. S. Aliev, S. S. Musayeva, F. Y. Jafarli, O. A. Aliyev, M. B. Babanly, The phase relationship in the Bi-Bi$_2$S$_3$-BiI$_3$ ternary subsystem, Chem. Problems, №4, 2012, p. 444-449

21. T. Okuda, T. Maegawa, M. Ye, K. Shirai, T. Warashina, K. Miyamoto, K. Kuroda, M. Arita, Z. S. Aliev, I. R. Amiraslanov, M. B. Babanly, E. V. Chulkov, S. V. Eremeev, A. Kimura, H. Namatame, M. Taniguchi, Experimental evidence of hidden topological surface states in PbBi$_4$Te$_7$, Phys. Rev. Lett. 111, 2013, p. 206803.

22. G. I. Ibadova, Z. S. Aliyev, M. B. Babanly, The interactions between the components in the YbTe-SnTe-Sb$_2$Te$_3$ system, XII int. conf. on crystal chemistry of intermetallic compounds, Lviv, Ukraine, 2013, p. 75

23. K. D. Rasulova, Z. S. Aliev, U. A. Kulieva, M. B. Babanly, Relationship of ytterbium telluride with ternary phases of the system SnTe-Bi$_2$Te$_3$, News of BSU, №4, 2013, p. 13-18

24. Z. S. Aliev, K. D. Rasulova, G. I. Ibadova, F. M. Sadigov, Phase equilibria in the YbTe-Sb$_2$Te$_3$-Bi$_2$Te$_3$ system, X int. Kurnakov meeting on physicochemical analysis, Samara, Russia, 2013, p. 216-217

25. D. Niesner, S. Otto, V. Hermann, T. Fauster, T. V. Menshchikova, S. V. Eremeev, Z. S. Aliev, I. R. Amiraslanov, M. B. Babanly, P. M. Echenique, E. V. Chulkov, Bulk- and surface electron dynamics in a p-type topological insulator SnSb$_2$Te$_4$, Phys. Rev. B, 89, 2014, p. 081404.

26. Z. S. Aliev, K. D. Rasulova, I. R. Amiraslanov, J. C. Tedenac, M. B. Babanly, Phase diagram of the YbTe-Sb$_2$Te$_3$-Bi$_2$Te$_3$ quasi-ternary system, J. Alloys Compd. 589, 2014, p.399-404.

27. Z. S. Aliev, G. I. Ibadova, J. C. Tedenac, M. B. Babanly, Study of the YbTe-SnTe-Sb$_2$Te$_3$ quasi-ternary system, J. Alloys Compd. 602, 2014, p. 248-254.

28. Z. S. Aliev, S. S. Musayeva, F. Y. Jafarli, I. R. Amiraslanov, A. V. Shevelkov, M. B. Babanly, The phase equilibria in the Bi-S-I ternary system and thermodynamic properties of the BiSI and Bi$_{19}$S$_{27}$I$_3$ ternary compounds, J. Alloys Compd. 610, 2014, p. 522-528.

29. S. Roy, H. L. Meyerheim, A. Ernst, K. Mohseni, C. Tusche, M. G. Vergniory, T. V. Menshikova, M. M. Otrokov, A. G. Rybishchkova, Z. S. Aliev, M. B. Babanly, K. A. Kokh, O. E. Tereshchenko, E. V.

Chulkov, J. Schneider, J. Kirschner, Tuning the Dirac point position in Bi_2Se_3 (0001) via surface carbon doping, Phys. Rev. Lett. 113, 2014, p. 116802.

30. A. Politano, M. Caputo, S. Nappini, F. Bondino, E. Magnano, Z. S. Aliev, M. B. Babanly, A. Goldoni, G. Chiarello, E. V. Chulkov, Exploring the surface chemical reactivity of single crystals of binary and ternary bismuth chalcogenides, J. Phys. Chem. C 118, 2014, p. 21517-21522

31. Z. S. Aliev, K. D. Rasulova, J. C. Tedenac, M. B. Babanly, Phase equilibria in the $YbTe-Sb_2Te_3-Te$ system, J. Alloys Compd. 618, 2015, p. 167-171.

32. F. Pielmeier, G. Landolt, B. Slomski, S. Muff, J. Berwanger, A. Eich, A. A. Khajetoorians, J. Wiebe, Z. S Aliev, M. B. Babanly, R. Wiesendanger, J. Osterwalder, E. V. Chulkov, F. J. Giessibl,J. H. Dil, Response of the topological surface state to surface disorder in $TlBiSe_2$, New J. Phys. 17, 2015, p. 023067.

33. I. A. Nechaev, I. Aguilera, V. De Renzi, A. di Bona, A. L. Rizzini, A. M. Mio, G. Nicotra, A. Politano, S. Scalese, Z. S. Aliev, M. B. Babanly, C. Friedrich, S. Blugel, E. V. Chulkov, Quasiparticle spectrum and plasmonic excitations in the topological insulator Sb_2Te_3, Phys. Rev. B 91, 2015, p. 245123.

34. A. Politano, V. M. Silkin, I. A. Nechaev, M. S. Vitiello, L. Viti, Z. S. Aliev, M. B. Babanly, G. Chiarello, P. M. Echenique, E. V. Chulkov, Interplay of surface and Dirac plasmons in topological insulators: the case of Bi_2Se_3, Phys. Rev. Lett. 115, 2015, p. 216802.

35. Z. S. Aliev, K. D. Rasulova, S. Z. Imamalieva, M. B. Babanly, Phase equilibria in the $YbTe-Bi_2Te_3-Te$ system, Chemistry Journal, 5(2), 2015, p. 35-39

36. Z. S. Aliev, S. S. Musayeva, F. Y. Jafarli, M. B. Babanly, The phase equilibria in the $Sb-Sb_2S_3-SbI_3$ ternary system, Az. Chem. J. 2015, №2, p. 57-61

37. I. R. Amiraslanov, Z. S. Aliev, M B. Babanly, Physicochemical aspects of the design of topological insulators - a new class of functional materials, Az. Chem. J, 2015, №3, p. 6-38

38. K. D. Rasulova, Z. S. Aliyev, I. M. Yusibova, M. B. Babanly, Phase relations in the $YbTe-SnTe-Bi_2Te_3$ system, XV Int. conf. on physics and technology of thin films and nanosystems, Ivano-Frankivsk,

Ukraine, 2015, p. 376

39. Z. S. Aliev, I. R. Amiraslanov, E. V. Chulkov, M. B. Babanly, Thermodynamic and crystallographic aspects of the design of topological insulators based on tetradymite-like chalcogenide phases, All-Russ. sci. conf. "II Baikal Materials Science Forum", Ulan-Ude, Russia, 2015, v.1, p. 24

40. Z. S. Aliev, K. D. Rasulova, G. I. Ibadova, M. B. Babanly, Phase diagram of the YbTe-SnTe-Bi$_2$Te$_3$ system, XV All-Russ. conf. "high-purity substances and materials. obtaining, analysis, application", Nizhny Novgorod, Russia, 2015, p.115

41. Z. S. Aliev, I. R. Amiraslanov, E. V. Chulkov, M. B. Babanly, The role of phase diagrams in the design of topological insulators, Int. conf. "multifunctional chemical materials and technologies", Tomsk, Russia, 2015, v.1, p. 7-8

42. M. B. Babanly, E. V. Chulkov, Z. S. Aliev, I. R. Amiraslanov, Physicochemical aspects of the synthesis of topological insulators based on metal chalcogenides, VII All-Russ. conf. "Physicochemical processes in condensed matters and interphases - FAGRAN-2015", Voronej, Russia, 2015, p. 36

43. L. Viti, D. Coquillat, A. Politano, K. A. Kokh, Z. S. Aliev, M. B. Babanly, O. E. Tereshchenko, W. Knap, E. V. Chulkov, M. S. Vitiello, Plasma-Wave terahertz detection mediated by topological insulators surface states, Nano Lett. 16(1), 2016, p. 80-87.

44. M. Caputo, M. Panighel, S. Lisi, L. Khalil, G. Di Santo, E. Papalazarou, A. Hruban, M. Konczykowski, L. Krusin-Elbaum, Z. S. Aliev, M. B. Babanly, M. O. Otrokov, A. Politano, E. V. Chulkov, A. Arnau, V. Marinova, P. K. Das, J. Fujii, I. Vobornik, L. Perfetti, A. Mugarza, A. Goldoni, M. Marsi, Manipulating the topological interface by molecular adsorbates: adsorption of Co-Phthalocyanine on Bi$_2$Se$_3$, Nano Lett. 16(6), 2016, p. 3409-3414.

45. C. Lamuta, D. Campi, A. Cupolillo, Z. S. Aliev, M. B. Babanly, E. V. Chulkov, A. Politano, L. Pagnotta, Mechanical properties of Bi$_2$Te$_3$ topological insulator investigated by density functional theory and nanoindentation. Scr. Mater. 121, 2016, p. 50-55.

46. M. Papagno, S. V. Eremeev, J. Fujii, Z. S. Aliev, M. B. Babanly, S. K. Mahatha, I. Vobornik, N. T. Mamedov, E. V. Chulkov, D. Pacile, Multiple coexisting dirac surface states in three-dimensional

$PbBi_6Te_{10}$ topological insulator, ACS Nano, 10(3), 2016, p. 3518-3524.

47. C. Lamuta, A. Cupolillo, A. Politano, Z. S. Aliev, M. B. Babanly, E. V. Chulkov, M. Alfano, L. Pagnotta, Nanoindentation of single-crystal Bi_2Te_3 topological insulators grown with the Bridgman-Stockbarger method, Phys. Status Solidi B, 253, 2016, p. 1082-1086.

48. C. Lamuta, A. Cupolillo, A. Politano, Z. S. Aliev, M. B. Babanly, E. V. Chulkov, L. Pagnotta, Indentation fracture toughness of single-crystal Bi_2Te_3 topological insulator, Nano Res. 9(4), 2016, p. 1032-1042.

49. M. B. Babanly, E. V. Chulkov, Z. S. Aliev, I. R. Amiraslanov, Chemically design of 3D topological insulators based on metal chalcogenides, II Int. Turkic world conf. on chemical sciences and technologies, Skopje, Macedonia, 26-30 October, 2016, p. 78

50. M. M. Otrokov, A. Ernst, K. Mohseni, H. Fulara, S. Roy, G. R. Castro, J. Rubio-Zuazo, A. G. Ryabishchenkova, K. A. Kokh, O. E. Tereshchenko, Z. S. Aliev, M. B. Babanly, E. V. Chulkov, H. L. Meyerheim, S. S. P. Park, Geometric and electronic structure of the Cs-doped Bi_2Se_3 (0001) surface, Phys. Rev. B, 95, 2017, p. 205429.

51. Z. S. Aliev, S. S. Musayeva, M. B. Babanly, The phase relationships in the Sb-S-I system and thermodynamic properties of the SbSI, J. Phase Equilib. Diffus. 38, 2017, p. 887-896.

52. M. B. Babanly, E. V. Chulkov, Z. S. Aliev, A. V. Shevelkov, I. R. Amiraslanov, Phase diagrams in materials science of topological insulators based on metal chalcogenides, Russ. J. Inorg. Chem. 62(13), 2017, p. 1703-1729.

53. I. A. Shvets, I. I. Klimovskikh, Z. S. Aliev, M. B. Babanly, J. Sánchez-Barriga, M. Krivenkov, A. M. Shikin, E. V. Chulkov, Impact of stoichiometry and disorder on the electronic structure of the $PbBi_2Te_{4-x}Se_x$ topological insulator, Phys. Rev. B, 96, 2017, 235124.

54. R. Flammini, S. Colonna, C. Hogan, S. K. Mahatha, M. Papagno, A. Barla, P. M. Sheverdyaeva, P. Moras, Z. S. Aliev, M. B. Babanly, E. V. Chulkov, C. Carbone, F. Ronci, Evidence of β-antimonene at the Sb/Bi_2Se_3 interface, Nanotechnology, 29, 2018, p. 065704

55. Z. S. Aliev, I. R. Amiraslanov, M.-C. Record, J. C. Tedenac, M. B. Babanly, The YbTe-SnTe-Bi_2Te_3 system, J. Alloys Compd. 750,

2018, p. 887-894.

56. A. D. Pia, S. Lisi, O. Luca, D. Warr, M. M. Otrokov, Z. S. Aliev, E. V. Chulkov, R. G. Agostino, A. Arnau, M. Papagno, G. Costantini: TCNQ physisorption on the Bi_2Se_3 topological insulator, Chem-PhysChem, 19(18), 2018, p. 2405-2410

57. D. Pacile, S. V. Eremeev, M. Caputo, M. Pisarra, O. De Luca, I. Grimaldi, J. Fujii, Z. S. Aliev, M. B. Babanly, I. Vobornik, R. G. Agostino, A. Goldoni, E. V. Chulkov, M. Papagno, Deep insight into the electronic structure of ternary topological insulators: A comparative study of $PbBi_4Te_7$ and $PbBi_6Te_{10}$, Phys. Status Solidi RRL, 12(12), 2018, p. 1800341

58. A. N. Mammadov, Z. S. Aliev, M. B. Babanly: Study of the uncertainty heterogeneous phase equilibria areas in the binary YbTe-SnTe alloy system, Chapter in XIII Int. conf. on theory and application of fuzzy systems and soft computing - ICAFS-2018, Warsaw, Poland, August 27-28, p. 815

59. Z. S. Aliev, I. R. Amiraslanov, D. I. Nasonova, A. V. Shevelkov, N. A. Abdullayev, Z. A. Jahangirli, E. N. Orujlu, M. M. Otrokov, N. T. Mamedov, M. B. Babanly, E. V. Chulkov, Novel ternary layered manganese bismuth tellurides of the $MnTe-Bi_2Te_3$ system: synthesis and crystal structure, J. Alloys Compd. 789, 2019, p. 443-450.

60. C. Hogan, K. Holtgrewe, F. Ronci, S. Colonna, S. Sanna, P. Moras, P. M. Sheverdyaeva, S.Mahatha, M. Papagno, Z. S. Aliev, M. Babanly, E. V. Chulkov, C. Carbone, R. Flammini, Temperature driven phase transition at the antimonene/Bi_2Se_3 van der Waals heterostructure, ACS Nano, 13, 2019, p.10481-10489

61. Z. S. Aliev, E. C. Ahmadov, D. M. Babanly, I. R. Amiraslanov, M. B.Babanly, The Bi_2Se_3-Bi_2Te_3-BiI_3 system: synthesis and characterization of the $BiTe_{1-x}Se_xI$ solid solutions, Calphad, 66, 2019, p. 101650

62. M. M. Otrokov, I. I. Klimovskikh, H. Bentmann, D. Estyunin, A. Zeugner, Z. S. Aliev, S. Gaß, A. U. B. Wolter, A. V. Koroleva, A. M. Shikin, M. Blanco-Rey, M. Hoffmann, I. P. Rusinov, A. Yu. Vyazovskaya, S. V. Eremeev, Yu. M. Koroteev, V. M. Kuznetsov, F. Freyse, J. Sánchez-Barriga, I. R. Amiraslanov, M. B. Babanly, N. T. Mamedov, N. A. Abdullayev, V. N. Zverev, A. Alfonsov, V. Kataev, B. Büchner, E. F. Schwier, S. Kumar, A. Kimura, L. Petaccia, G. Di

Santo, R. C. Vidal, S. Schatz, K. Kißner, M. Ünzelmann, C. H. Min, S. Moser, T. R. F. Peixoto, F. Reinert, A. Ernst, P. M. Echenique, A. Isaeva, E. V. Chulkov, Prediction and observation of an antiferromagnetic topological insulator, Nature, 576, 2019, p. 416-422

63. I. A. Shvets, I. I. Klimovskikh, Z. S. Aliev, M. B. Babanly, F. J. Zuniga, J. Sanchez-Barriga, M. Krivenkov, A. M. Shikin, E.V. Chulkov, Surface electronic structure of the wide band gap topological insulator $PbBi_4Te_4Se_3$. Phys. Rev. B, 100, 2019, p. 195127

64. Z. S. Aliev, Novel variable phases in the quaternary Pb-Bi-Te-Se system along the $PbBi_2Te_4$-"$PbBi_2Se_4$" isopleth section, Az. Chem. J, № 4, 2019, p. 54-58.

65. Z. S. Aliev, Synthesis and characterization of the $BiTe_{1-x}Se_xI$ solid solutions series, AJP Fizika, № 2(XXV), 2019, Section: En, p. 37-40.

66. Z. S. Aliev, The A^V-B^{VI}-I ternary systems: a brief review on the phase equilibria, Condensed Matter and Interphases, № 21(3), 2019, p. 338-349

67. Z. S. Aliev, The solid-state phase diagram of the $PbTe$-$PbSe$-Bi_2Se_3-Bi_2Te_3 reciprocal system // New Materials, Compounds and Applications, №3(3), 2019, p.180-186

68. Z. S. Aliev, The phase equilibrium in the Bi_2Se_3-BiI_3-Se system, Transaction of Azerbaijan Higher Technical Educational Institutes, №21(6), 2019, p. 41-46

69. D. A. Estyunin, I. I. Klimovskikh, A. M. Shikin, E. F. Schwier, M. M. Otrokov, A. Kimura, S. Kumar, S. O. Filnov, Z. S. Aliev, M. B. Babanly, E. V. Chulkov, Signatures of temperature driven antiferromagnetic transition in the electronic structure of topological insulator $MnBi_2Te_4$. APL Mater. 8, 2020, p. 021105

70. I. Grimaldi, D. Pacile, S. V. Eremeev, O. De Luca, A. Policicchio, P. Moras, A. K. Kundu, Z. S. Aliev, P. Rudolf, R.G. Agostino, E. V. Chulkov, M. Papagno, Electronic band structure of three-dimensional topological insulators with different stoichiometry composition. Phys. Rev. B, 102, 2020, p. 085118

71. K. Holtgrewe, S. K. Mahatha, P. M. Sheverdyaeva, P. Moras, R. Flammini, S. Colonna, F. Ronci, M. Papagno, A. Barla, L. Petaccia, Z. S. Aliev, M. B. Babanly, E. V. Chulkov, S. Sanna, C. Hogan, C. Carbone, Topologization of β-antimonene on Bi_2Se_3 via proximity effects. Sci. Report, 10, 2020, p. 14619

72. A.M. Shikin, D.A. Estyunin, I.I. Klimovskikh, S. Filnov, E.F. Schwier, S. Kumar, K. Myamoto, T. Okuda, A. Kimura, K. Kuroda, K. Yaji, S. Shin, Y. Takeda, Y. Saitoh, Z. S. Aliev, N. T. Mamedov, M. B. Babanly, I. R. Amiraslanov, M. M. Otrokov, S. V. Eremeev, E. V. Chulkov, Nature of the Dirac gap modulation and surface magnetic interaction in axion antiferromagnetic topological insulator $MnBi_2Te_4$. Sci. Report, 10, 2020, p. 13226

73. I. I. Klimovskikh, M. M. Otrokov, D. Estyunin, S. V. Eremeev, S. O. Filnov, A. Koroleva, E. Shevchenko, V. Voroshnin, I. P. Rusinov, M. Blanco-Rey, M. Hofmann, Z. S. Aliev, M. B. Babanly, I. R. Amiraslanov, N. A. Abdullayev, V. N. Zverev, A. Kimura, O. E. Tereshchenko, K. A. Kokh, L. Petaccia, G. Di Santo, A. Ernst, P. M. Echenique, N. T. Mamedov, A. M. Shikin, E. V. Chulkov, Tunable 3D/2D magnetism in the $(MnBi_2Te_4)\cdot(Bi_2Te_3)_m$ topological insulators family. npj Quantum Materials, 5, 2020, 54

74. M. Nurmamat, K. Okamoto, S. Zhu, T. V. Menshchikova, I. P. Rusinov, V. O. Korostelev, K. Miyamoto, T. Okuda, T. Miyashita, X. Wang, Y. Ishida, K. Sumida, E. F. Schwier, M. Ye, Z. S. Aliev, M. B. Babanly, I. R. Amiraslanov, E. V. Chulkov, K. A. Kokh, O. Tereshchenko, K. Shimada, S. Shin, A. Kimura, Topologically nontrivial phase-change compound $GeSb_2Te_4$, ACS Nano, 14(7), 2020, p. 9059-9065

75. M .B. Babanly, Z. S. Aliev, Chemical design of magnetic topological insulators, International conference on actual problems of chemical engineering (APCE-2020), dedicated to the 100th anniversary of the Azerbaijan State Oil And Industry University, Baku, Azerbaijan, 2020, December 24-25, p. 18